Final Report

Radar Studies of the Moon

28 February 1970

Prepared for the National Aeronautics and Space Administration
under Contract NAS 9-7830 by

Lincoln Laboratory

MASSACHUSETTS INSTITUTE OF TECHNOLOGY

Lexington, Massachusetts

Final Report

Radar Studies of the Moon

28 February 1970

Issued 17 September 1970

Prepared for the National Aeronautics and Space Administration
under Contract NAS 9-7830 by

Lincoln Laboratory

MASSACHUSETTS INSTITUTE OF TECHNOLOGY

Lexington, Massachusetts

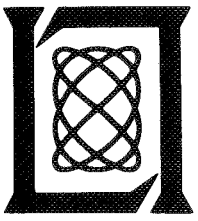

The work reported in this document was performed at Lincoln Laboratory, a center for research operated by Massachusetts Institute of Technology. This work was sponsored by the National Aeronautics and Space Administration under Contract NAS 9-7830.

FOREWORD

This report marks the termination of the backscatter measurement phase of the work being carried out under Contract NAS 9-7830.

The experimental results of this part of the program are a set of highly resolved maps of the radar backscattering properties of the lunar surface, of both the expected and the depolarized return, on a scale of about 2 km (about 1 arc-second at the surface of the earth). The report contains a description of these results and a brief outline of the equipment and methods that were used. A section on the theory of radar backscatter provides the framework for the final section containing analyses of the surface characteristics of a number of proposed and alternate Apollo landing sites.

The next phase of the contract is a study of lunar topography at improved resolution. This work will be covered in Quarterly Progress Report No. 7, dated 15 June 1970.

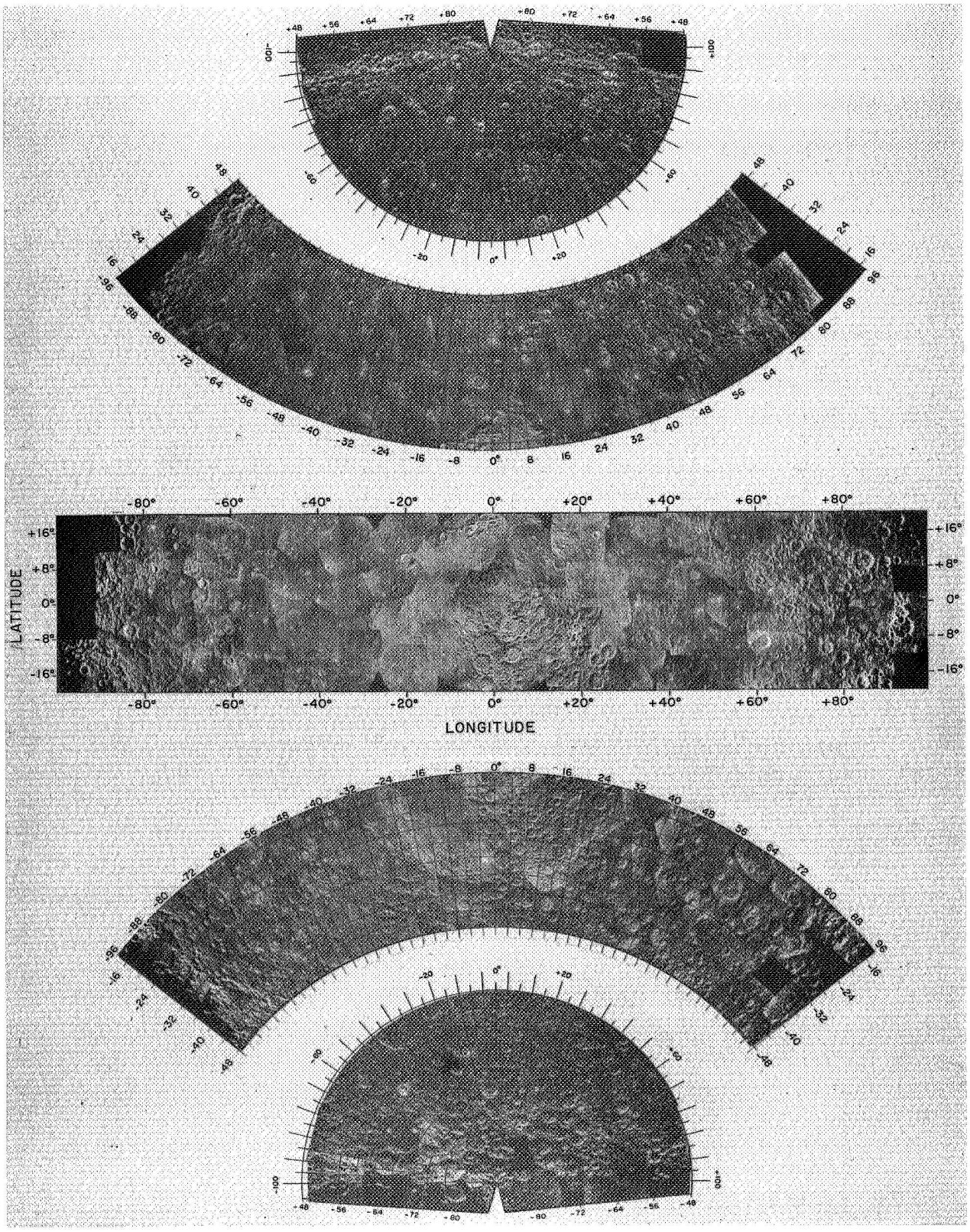

Polarized radar backscatter from the lunar surface.
Haystack planetary radar, 3.8-cm wavelength.

CONTENTS

MAPPING OF THE RADAR BACKSCATTER CHARACTERISTICS OF THE LUNAR SURFACE

I. INTRODUCTION

Observations of the moon by radar over the past two decades have produced much information on the average backscattering properties of the surface of the moon over a wide range of wavelengths. The existence of a strong central glint to the radar return has been interpreted as reflections from a smooth, undulating surface, and has permitted the average slope of this surface to be calculated. On the other hand, the existence of a diffuse component in the returns at some distance from the center of the disk has been interpreted as originating in wavelength-sized structure on the surface, presumably from rocks on or near the surface. This interpretation has been strengthened by measurements of the depolarization of lunar ehcoes[1*] and by the discovery of anomalously enhanced radar echoes from the region of the crater Tycho,[2-4] a crater known to be bright on optical photographs, to possess an extensive system of surface rays, and to possess a strong thermal enhancement. Several earlier studies have included measurements of the radar-moon with high resolution and have provided information about the surface structure in considerable detail.[4-5]

Since radar returns are presumed to arise from centimeter- and decimeter-sized irregularities, such data were of some immediate interest to those planning lunar landing systems. Accordingly, a program of radar measurements of the moon was funded by NASA in 1965-1967 at the Haystack Research Facility. The results of the study were described in a two-volume Final Report (NASA Contract NSR 22-009-106, dated 31 August 1967 and 18 April 1968) and included a set of high-resolution radar measurements of an equatorial belt 140° wide in longitude and 32° in latitude.

These radar maps revealed the existence of a number of anomalously strong backscattering regions, some of which were correlated with bright optical features (although none with a relative optical enhancement as great as the radar enhancement) and some with thermally anomalous regions.[6] It appeared that the radar data might permit differentiation between surface features that are not so clearly differentiable by other means.

An extended program of radar measurements was then undertaken with considerable further support from NASA, the results of which are being reported in this report. The original measurements were extended to cover the entire earthside hemisphere of the moon. The radar system was upgraded to permit the simultaneous measurement of both senses of circularly polarized backscatter. Particular care was taken with amplitude calibration in order to permit comparison of measurements that were widely spaced in time as well as selenographic position. The Doppler and timing systems were modified for improved setting accuracy. Frequent measurements of the area of the first radar echo ("leading edge") were made during each observing period to check the range and Doppler ephemerides which were still in some question in the earlier program.

In addition to the radar data, this report contains a certain amount of interpretation of parts of the moon's surface, including mainly the proposed primary and alternate Apollo sites that are

* References are listed on p. 45.

expected to be of most immediate interest to NASA. The interpretation is included as an illustration of one method of utilizing the radar data for analysis of surface structure. It is only a first effort on the part of the present investigators to exploit the great mass of information presented here. It is anticipated that further work will be carried out by the present investigators as time and funds permit, and that other investigators will also be encouraged to make use of the data.

In the next section, the experiment and the subsequent normalization of the measurements are described in detail. Enough information is included to permit an independent evaluation of the accuracy of the measurements and hence the conclusions in this report. Section III outlines the theory of the backscattering of electromagnetic energy from various models of the lunar surface. That section provides the justification for the data analyses in this report and may provide a framework for future theoretical investigations. Section IV, finally, presents the data and summarizes the interpretations that were alluded to above.

II. EXPERIMENT

The purpose of the measurements to be described was to obtain highly resolved maps of the backscattering capability at a wavelength of 3.8 cm of the entire earthside hemisphere of the moon. The intended resolution of 2.5 km is comparable to that obtainable at optical wavelengths with earth-based telescopes. The signals at the two widely different wavelengths are presumably scattered back by two different scales of surface structure. The radar resolution was obtained by the coherent-pulse analysis technique ("range-Doppler mapping"), using the Haystack radar and post-processing system with parameters as listed in Table I.

In the coherent-pulse method, the location of a given element on the moon's surface depends only on the range, range-rate, and various sources of apparent rotation. The resolution afforded by the radar beam serves only as a window through which may be admitted the signals from the appropriate range- and frequency-resolved elements. Figure 1 should help to make this situation clear. The short pulse from a wide-beam radar illuminates a circular (range-) ring (disregarding any effects of topography) on the moon at any instant of time. Since the Haystack radar has a narrow beam, only that portion of the range-ring within the projection of the beam actually receives energy. The integrated backscattered signal from this ring arrives back at the radar at a predictable time later and provides resolution in one direction. At the same time, all backscattered signals have been Doppler shifted by an amount equal to the sum of two terms: one constant term resulting from the radial velocity of the center of mass of the moon, and one term linearly proportional to the distance of the backscattering element from the libration plane, i.e., the plane containing the apparent libration axis and the subradar point.* If the returned signals are frequency-analyzed, therefore, the signal in any narrow band that is offset from the frequency of the subradar point is the integrated backscattered signal from a strip that is offset by the corresponding distance from the libration plane. This provides resolution in another direction, and good two-dimensional resolution is obtained when the libration axis passes through or nearly through the area being measured (provided that this area does not also contain the lunar equator).

In order to insure efficient coverage of the near side of the moon, a system of sub-areas was set up whose boundaries paralleled the resolution cells of the range and Doppler measurements. The earthside hemisphere was divided into nine concentric ZAC (Zenith-Azimuth Coordinate) rings, each of 10° width, with a tenth ring to cover areas which are only temporarily

* The subradar point is the intersection of the surface of the moon with the line joining the radar and the center of mass of the moon. In mountainous terrain, it may not produce the first radar return, but its radial velocity is identical with that of the center of mass.

TABLE I

RADAR PARAMETERS FOR LUNAR OBSERVATIONS

Wavelength (frequency)	Approximately 3.8 cm (7840.0 GHz)
Polarization	
Transmitted	Right-circular
Received	Simultaneous left (polarized) and right (depolarized) circular
TRANSMITTER	
Power	200 kW (peak)
Pulse Length	3, 4, 5, 7, 10, or 13 μsec
Interpulse Period	25-90 msec (adjusted for 2.3-km frequency resolution on the surface)
Frequency Standard	Hydrogen maser or rubidium standard
Utilization	All transmitter, receiver, and timing functions
Precision	$1{:}10^{11}$
RECEIVER	
System Temperature	
Polarized	45°K (sky); 180°K (moon)
Depolarized	75°K (sky); 210°K (moon)
Operating Frequency	7840.0 GHz + Doppler offset to center of ZAC-area
Setting Accuracy	±0.01 Hz
Resetting Interval	10 msec
ANTENNA	
Gain	66 dB
Effective Area ($= \eta\pi R^2$)	460 m^2
Beamwidth (one-way)	4 arc-min (full-width at half-power)
Pointing and Following Accuracy	±20 arc-sec
REAL-TIME PROCESSING	
Computer	CDC-3300
Samples per Received Pulse	190
Calibration Samples per Interpulse	26 (20 usable)
Sample Interval	3-13 μsec (to match transmitter pulsewidth)
Timing of Samples	Sample 95 (of 190) tracks center of ZAC-area

TABLE I (Continued)

POST-PROCESSING	
Number of Pulses Coherently Analyzed	256
Duration of Coherent Integration Period (CIP)	6 to 26 sec (= 256 × interpulse period)
Number of CIP's per Map	85 ± 5
Precision of Backscatter Values	11% rms
NORMALIZATION PARAMETERS	
Two-Way Beam Shape	$\exp[-1.39\,r^2/2.2^2]$
Background Noise Level per Received Pulse	As measured at 1.0 msec prior to first lunar echo
Scattering law	Depolarized: $S(\theta) = \cos(\theta)$
	Polarized: see Eq. (1)
Area of Resolution Cell	
Range-Doppler Coordinates	Rectangular, = pulsewidth × frequency resolution
Lunar Surface Coordinates	Same, projected onto spherical lunar surface
Additional Corrections	Transmitted power
	Earth-moon distance
	DC and AC background levels
	Receiver gain
MAPPING PARAMETERS	
Observed Coordinates	Range-Doppler
Projected Surface	1738.0-km sphere
Final Map Projections	Mercator, Lambert conformal, polar stereographic
Precision of Absolute Locations	±4 km (rms)
	±20 km (occasional peaks)

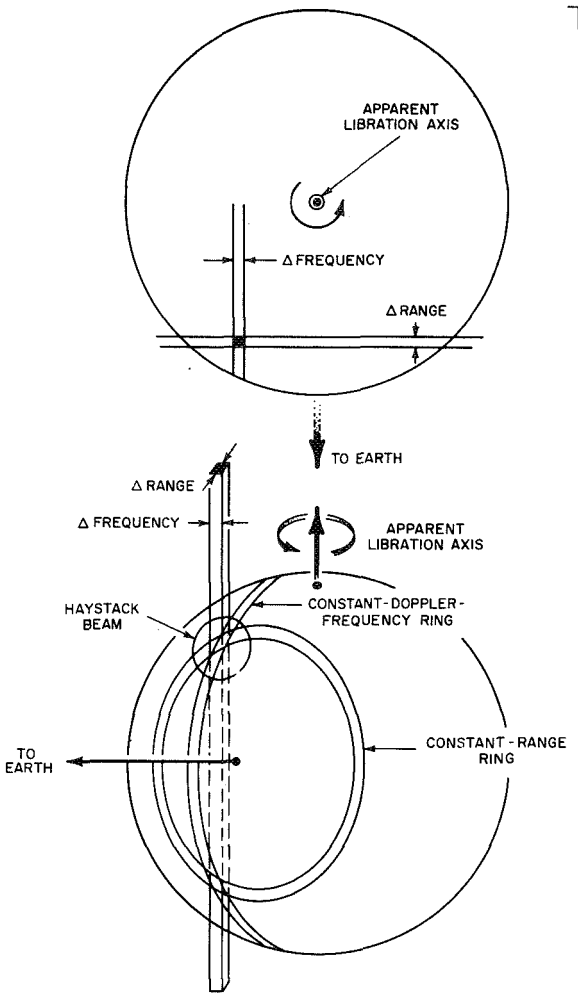

Fig. 1. Range-Doppler resolution schematic diagram.

brought into view by libration. Each ring was further subdivided to produce ZAC-areas containing roughly equal areas of the moon's surface. A map of the ZAC-area system appears in Fig. 2.

A. Positioning of the Maps

During each observation, the radar receiver (diagrammed in Fig. 3) was adjusted to follow continuously the predicted values of range and Doppler frequency for the center of the area being observed. This center point then became the reference for the remainder of the map. Any time-varying error in the prediction ephemerides would result in a blurring of the map, whereas a constant error would only displace the map in the range or Doppler directions. Errors in the predicted selenographic position of the subradar point, which would have rotated the map with respect to the moon's surface, and errors in the apparent angular velocity of libration, which would have affected the scale in the frequency direction, were considered to be negligibly small.*

* A recent closer investigation of current libration ephemerides suggests that they may, in fact, be a source of error of the same order as the center-of-mass ephemerides.

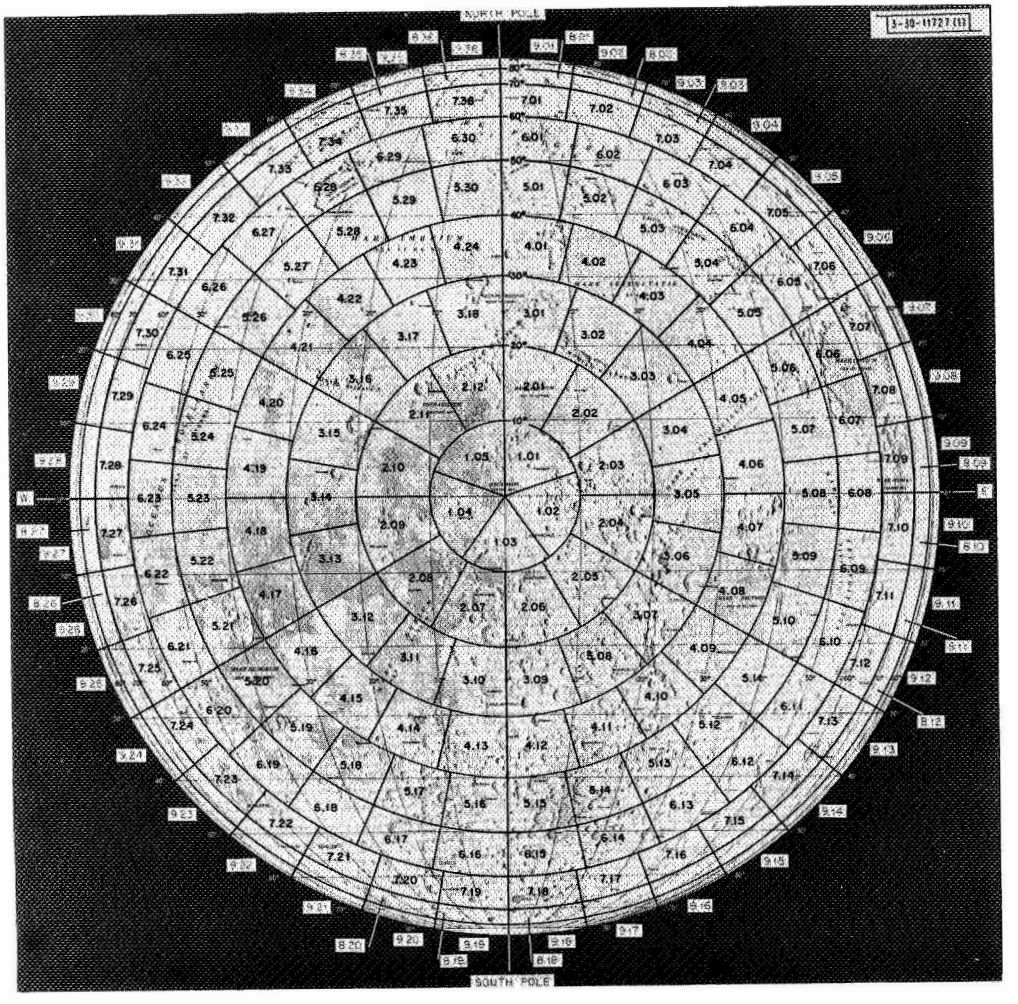

Fig. 2. ZAC-area chart.

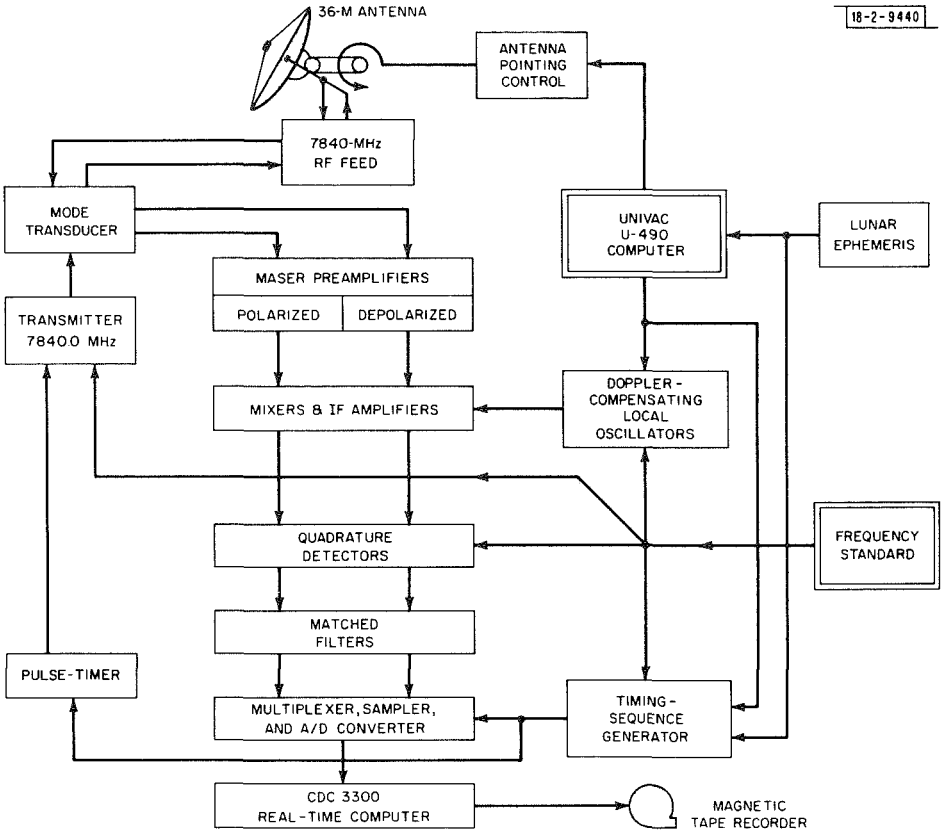

Fig. 3. Radar system block diagram.

The range and range-rate of the center of mass of the moon were predicted, respectively, from the Nautical Almanac (i.e., Brown's theory) and from Brown's theory as corrected by Eckert, et al.[7] Calibration measurements were made of the central part of the disk (the leading edge) at frequent intervals during each day's observations. These leading-edge observations were frequency-analyzed like a standard map and furnished a check of the predicted Doppler frequency and range of the subradar point. No attempt was made either in the calibration checks or in the reduction of the maps themselves to compensate for the lunar topography; in all cases, a radius of 1738.0 km was assumed. The total discrepancy in range between predictions and observations was less than 6 km, and all but 0.5 to 1.0 km were invariably the result of known discrepancies between our working range-prediction ephemeris and the best-known values for range, together with known variations in topography near the subradar point. These calibration measurements thus may provide the raw data for future detailed investigation of the lunar topography surrounding the mean subearth point.

The observed discrepancies in the frequency were also apparently due mainly to the effects of topography. Quantitatively, the discrepancies were less than one frequency-resolution cell (frequency box). The size of one frequency box was set to approximately 2.3 km on the moon's surface by an appropriate selection of the transmitter interpulse period.

The maximum error, then, in the position of a map is about 7.5 km on the range-Doppler plane, with most maps being located substantially more accurately. The maps, however, are projected from the range-Doppler plane onto an assumed 1738-km sphere, and topographic

variations will result in a total maximum location error of as much as 20 km near the center of the disk, or about 0.7° selenographic.

The positional accuracy quoted is based in part on comparisons between overlapping ZAC maps, where a difference in the orientation of the libration axis between adjacent maps leads to a difference in the observed distortion caused by topography. Another source for position measurement was the set of Lunar Aeronautical Charts (USAF-ACIC, various dates 1958-1969). The major difficulty in the use of these LAC charts is that near the limb their accuracy (there is no elevation information near the limbs) was much worse than the apparent accuracy of the radar maps, while conversely near the center of the disk the radar maps were most susceptible to distortion by both topography and errors in the prediction ephemerides.

For position measurements with the highest accuracy, the feature of interest can be located precisely on the ZAC maps with respect to other recognizable features.

Two sets of radar maps will be described in this report. In the set consisting of the series of individual ZAC maps, the coordinate grids are calculated from the predicted position and velocity of the moon during the radar observation. These are most nearly correct. The other set contains an assembly of the individual maps into mosaics. Here there was a confusing misalignment of the surface features between adjacent maps for the reasons outlined above. The mosaic maps were therefore assembled without coordinate grids by matching the surface features, and one-piece grid systems were applied to the completed maps afterward. These mosaics are intended only as finding charts; for more precise location of features, the individual ZAC maps should be referred to.

B. Normalization and Projection of the Maps

Several stages of normalization were employed on the data during the later parts of the computer processing. The initial processing step, performed on the string of time-samples (see Fig. 4) stored on magnetic tape during a run, was the separation of the sample string into blocks of 256 receiver pulses, each pulse consisting of 190 closely spaced time-samples of the radar

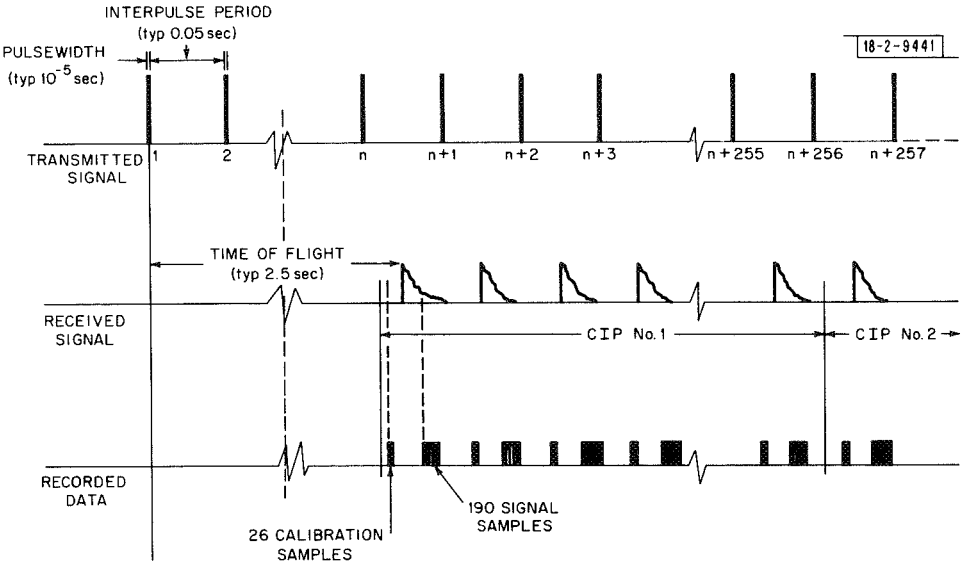

Fig. 4. Timing of coherent-pulse radar measurements.

return. These blocks were further rearranged into 190 strings of 256 samples each, and each string, corresponding to a given range (delay), was Fourier-analyzed into 256 frequency cells. The result was a single range-Doppler-resolved map of 190×256 independent backscatter values.

The power in each cell is expected to fluctuate because of the random phase of the signals from the individual scatterers within each cell. The fluctuation in the signal is independent of any noise contributed by the receiver, and can be reduced by taking the mean of a number of independent observations. A compromise is necessary between the precision of the backscatter value and the duration of the observation interval and especially of the later computer-processing time. We chose to measure 85 ± 5 separate range-Doppler maps during each observation period, insuring an rms error of about 11 percent in the final value of backscattered power in each cell.

The elemental maps were summed until the calculated location of the edges of a given map were out of alignment with the first map by one cell-width in any direction. The result was a partial-sum map that was normalized and projected onto the selected cartographic coordinate system. The remaining elemental maps were summed in the same way, with each partial sum being projected independently onto the same cartographic grid and the result, after normalization, summed into the final integrated map. The cartographic projections are the same as those of the LAC series. A Mercator projection was employed for latitudes less than 16°, two different Lambert conformal projections from 16° to 48° and 48° to 80°, and a polar stereographic projection for the remaining polar caps.

The normalization performed on each of the partial sums was intended to compensate for the parameters of the radar system, the moon's position, the size and shape of the range-Doppler resolution cells on the moon, and the expected average variation of the backscattered signal with angle of incidence. Let us take these factors in the given order.

1. Radar Parameters

Corrections for transmitter power and earth-moon distance are self-explanatory. The range-Doppler cells were assumed to be rectangular with dimensions equal to the sample interval in range and to the frequency-spacing in Doppler. This gives a proper correction relative to the other observations, although the true area of the resolution cell will be modified by the non-ideal shapes of the filters in both range and Doppler. The filter passbands required special compensation as outlined below. The rectangular cell was projected onto the moon's surface to get the cell-size correction factor in terms of per-unit surface area.

The noise and gain of the radar receiver were measured during the observation via an extra burst of 26 samples that preceded each received signal-pulse (Fig. 4). A gas discharge calibration noise source was switched on during the first half of these samples to provide a means for measuring the system temperature under operating conditions. Noise temperatures were also measured by more conventional methods once or twice during each observation period, either on or off the moon. The two types of noise-temperature measurement gave consistent values most of the time, except when the operation of the transmitter had some effect on the system noise level.

The system temperature was compared with the measured baseline signal (the output power from the receiver in the absence of a radar return) to determine a gain-correction factor. The baseline power was also subtracted from the moon signals to obtain the signal strength above the noise level. In the case of the resolution cells with zero-frequency offset, the residual DC components from the detectors were removed by comparison of the average zero-frequency signals with the average of the +1 and −1 frequency-box signals.

2. Geometric Parameters

The narrow beam of the radar was essential for the elimination of the range-Doppler ambiguity point. As can be seen in Fig. 1, the range-Doppler resolution cell has a rectangular cross section but unlimited length and will generally intersect the spherical lunar surface in two places. One of these complementary intersections is not wanted, and is generally far outside the beam of the antenna except when an area near the libration equator is being measured. For each data point on each ZAC map, the distance of the complementary point from the center of the beam was calculated. If this distance was less than 1.5 half-power two-way beamwidths, the data point was discarded.

Since the beam of the antenna is comparable in size with a ZAC-area, the strength of the signal as received was modified by the beam pattern of the antenna. The beam pattern is closely approximated (better than 2 percent) by a Gaussian function with a half-amplitude width of 2.9 arc-min out to a radius of at least 1.5 half-power beamwidths. Signals within 1.4 half-power beamwidths (2.1 arc-min) of the center of the beam were corrected for the Gaussian beam shape; signals beyond 1.4 beamwidths were discarded because of low signal-to-noise ratio and reduced accuracy in our knowledge of the shape of the radar beam.

3. Scattering Law

Perhaps the most important modification of the radar measurements, in that it has the greatest effect on the details of the backscatter maps, is the strong limb-darkening function (scattering law) of the moon at radar wavelengths. This effect has been known for some time

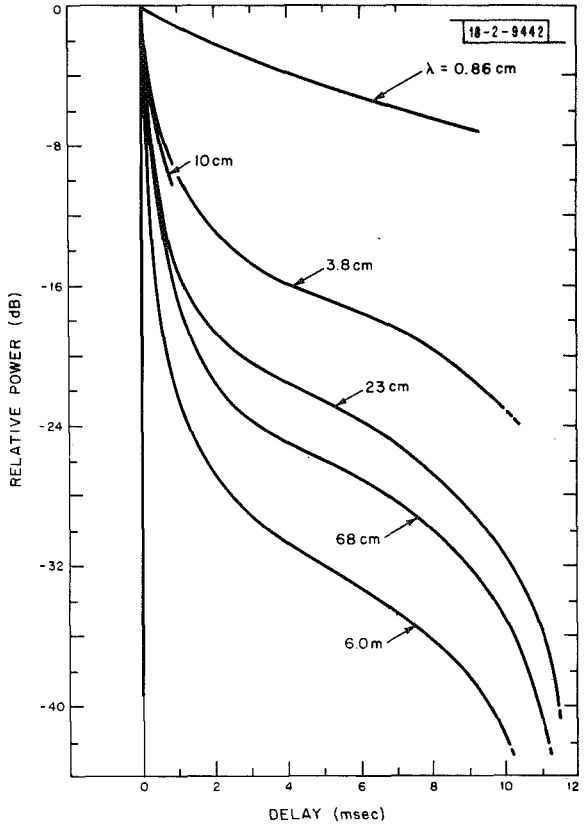

Fig. 5. Lunar radar scattering laws, various wavelengths.

and will be discussed in detail in the next section. The power scattered back per unit area of surface is plotted in Fig. 5 at a number of wavelengths, including 3.8 cm (Ref. 1). For simplicity, the following analytic approximations were used:

$$S(\Theta) = \begin{cases} \Theta \leqslant 59.7°: & \dfrac{\cos(\Theta)}{[\cos(\Theta) + \sin(\Theta)/0.35]^3} \\ \Theta > 59.7°: & \dfrac{\cos(\Theta)}{\left[\left(\dfrac{\sin(\Theta)}{0.295}\right)^2 + \cos^2(\Theta)\right]^{3/2}} \end{cases} , \tag{1}$$

where Θ is the angle of incidence of the point being normalized, and $S(\Theta)$ is the approximation to the scattering law of Fig. 5. Representative values of $S(\Theta)$ appear in Table II, together with the corresponding values from the earlier measurements for comparison. The results of the present measurements have been normalized to this function to emphasize those deviations from the mean or typical scattering which we shall associate with features. Large-scale (i.e., hundreds of km) deviations from the normalized scattering law represent either discrepancies between the current measurements and those previously reported, or real deviations from the over-all average by different classes of terrain or by specific lunar features. Small-scale deviations (i.e., tens of km or less) have already been observed in earlier high-resolution radar measurements[3,4] and show up profusely over all the maps. They may result from a number of different local surface anomalies to be discussed in greater detail in the subsequent section.

This discussion of scattering law so far applies only to the polarized return, defined as the component with that polarization expected in a wave reflected by a smooth metallic surface. The Haystack radar transmits a right-circularly polarized wave, so that the polarized return is the left-circular component. During the present measurements, both the polarized and the depolarized components of the backscattered wave were recorded simultaneously and subsequently processed into maps in the identical manner. The only difference was in the normalization to an assumed scattering law. In this case, for the depolarized signal,

$$S_D(\Theta) = \cos(\Theta) , \tag{2}$$

where $S_D(\Theta)$ is the average backscattered depolarized power per unit surface area. This scattering function has been previously reported for measurements at 23-cm wavelength[1] (see Fig. 6) and also at 70 cm (Ref. 4). It was adopted as a best estimate of the scattering law at 3.8 cm, in the absence of any other observational information.

C. Reliability of the Data

After the normalizations described above, the average of the present measurements proved to be almost independent of angle of incidence, thereby supporting the assumed scattering laws. An anomaly observed at the smaller angles was found to result from the difference in the response of the signal-processing system to the broadband incoherent calibration source as compared to the coherent backscatter signal from the moon. The major source of trouble originates in the non-ideal phase and amplitude response of the matched filters just in front of the analog-to-digital converters (Fig. 2). Because different pulsewidths and matched filters were used to achieve the same surface resolution at different distances from the subradar point, a different calibration had to be applied to measurements at each of the pulsewidths.

TABLE II

RADAR CROSS SECTION PER UNIT SURFACE AREA (dB)

Delay (μsec)	θ (deg)	S(θ) Observed	S(θ) Analytic Approximation	Delay (μsec)	θ (deg)	S(θ) Observed	S(θ) Analytic Approximation
10	2.38	−0.83	−2.03	2250	36.29	−14.18	−13.44
20	3.37	−1.43	−2.59	2500	38.33	−14.58	−13.86
30	4.12	−1.98	−3.00	2750	40.28	−14.88	−14.26
40	4.76	−2.38	−3.33	3000	42.15	−15.23	−14.62
50	5.32	−2.73	−3.62	3250	43.96	−15.53	−14.97
60	5.83	−3.03	−3.87	3500	54.71	−15.83	−15.29
70	6.30	−3.33	−4.10	3750	47.41	−16.13	−15.60
80	6.73	−3.58	−4.31	4000	49.07	−16.38	−15.90
90	7.14	−3.83	−4.50	4250	50.68	−16.63	−16.18
100	7.53	−4.03	−4.68	4500	52.26	−16.93	−16.46
125	8.42	−4.58	−5.08	4750	53.81	−17.13	−16.73
150	9.22	−5.03	−5.43	5000	55.32	−17.43	−16.99
175	9.96	−5.38	−5.75	5250	56.81	−17.73	−17.24
200	10.65	−5.73	−6.03	5500	58.27	−17.98	−17.50
225	11.30	−6.03	−6.30	5750	59.71	−18.33	−17.74
250	11.92	−6.33	−6.54	6000	61.13	−18.63	−18.09
275	12.50	−6.68	−6.77	6250	62.53	−18.93	−18.44
300	13.06	−6.93	−6.98	6500	63.92	−19.33	−18.79
325	13.59	−7.23	−7.18	6750	65.29	−19.73	−19.14
350	14.11	−7.48	−7.37	7000	66.64	−20.13	−19.50
375	14.61	−7.73	−7.55	7250	67.98	−20.53	−19.85
400	15.09	−7.98	−7.72	7500	69.30	−21.03	−20.22
425	15.56	−8.23	−7.88	7750	70.62	−21.43	−20.59
450	16.01	−8.43	−8.04	8000	71.92	−21.88	−20.97
475	16.45	−8.63	−8.19	8250	73.21	−22.38	−21.37
500	16.88	−8.78	−8.33	8500	74.50	−22.88	−21.78
600	18.51	−9.33	−8.86	8750	75.78	−23.38	−22.22
700	20.01	−9.83	−9.33	9000	77.05	−23.98	−22.68
800	21.40	−10.23	−9.75	9250	78.31	−24.53	−23.18
900	22.72	−10.63	−10.13	9500	79.57	−25.33	−23.72
1000	23.97	−10.93	−10.48	9750	80.82	−26.03	−24.32
1100	25.15	−11.08	−10.80	10000	82.07	−26.93	−24.99
1200	26.29	−11.58	−11.10	10250	83.32	−27.93	−25.76
1300	27.39	−11.83	−11.38	10500	84.56	−29.33	−26.68
1400	28.44	−12.08	−11.65	10750	85.80	−30.83	−27.83
1500	29.46	−12.33	−11.90	11000	87.04	−32.03	−29.37
1750	31.88	−13.33	−12.47	11250	88.27	−32.83	−31.74
2000	34.15	−13.73	−12.98				

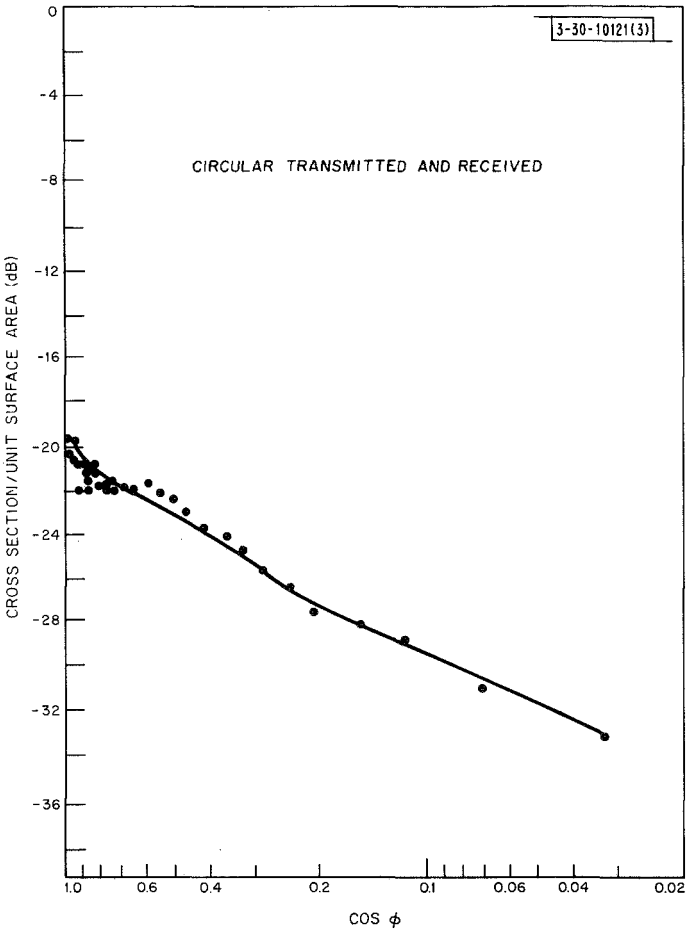

Fig. 6. Depolarized scattering law at 23-cm wavelength.

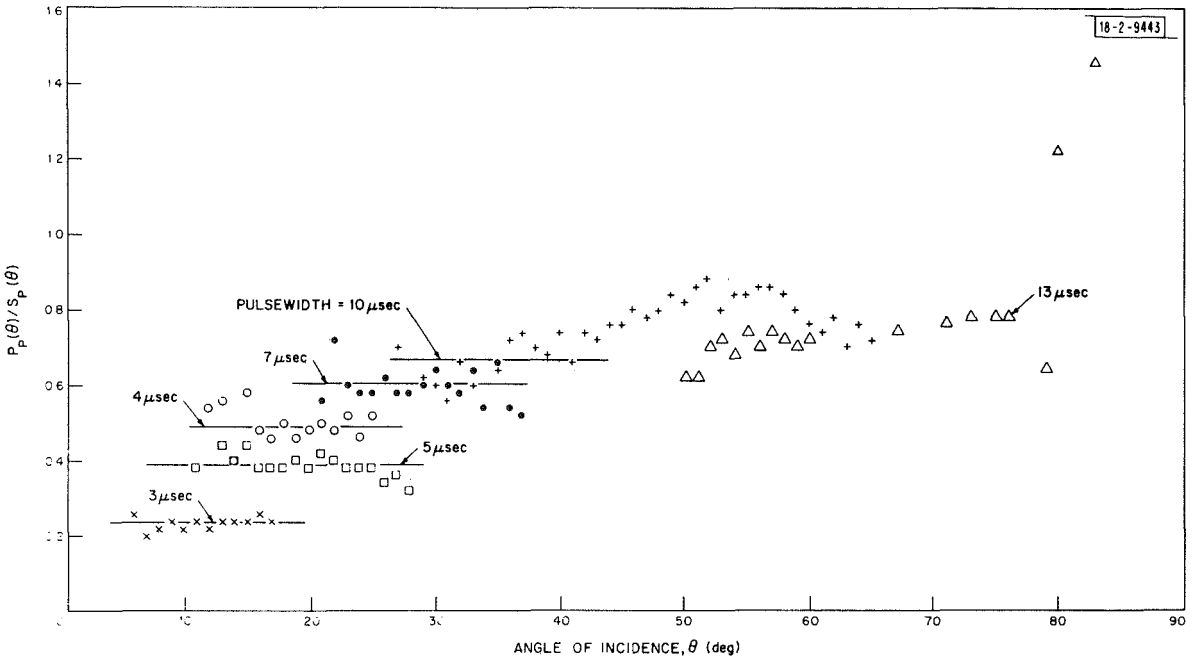

Fig. 7. Measured 3.8-cm polarized backscatter, $P_p(\theta)$, normalized to Eq. (1).

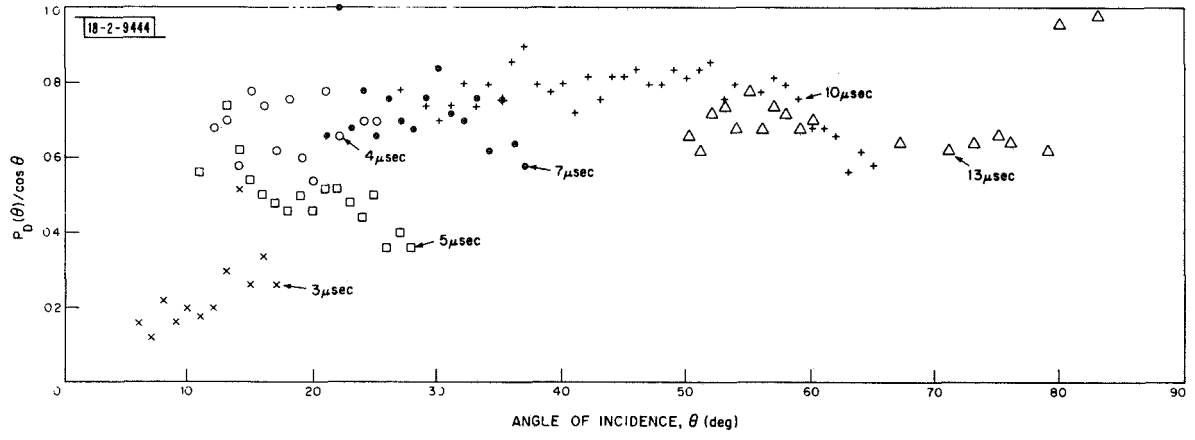

Fig. 8. Measured 3.8-cm depolarized backscatter, $P_D(\theta)$, normalized to cos θ.

The consistency of the results is demonstrated in Fig. 7, which is a series of graphs of the normalized polarized backscatter for each of the six pulsewidths used in the experiment before the pulsewidth calibrations were applied. The data have been corrected for the radar and geometry factors mentioned above and for the scattering law of Fig. 5. All corrections were based on positions and velocities of the moon's center-of-mass and on values for its calculated libration as explained in Sec. II-A.

After these purely mechanical corrections, each of the graphs in Fig. 7 shows essentially no angular dependence, indicating that the assumed scattering law is confirmed by these measurements except for the small positive slope for $\Theta > 40°$. The latter effect is artificial, being caused entirely by a deviation of the analytic expression [Eq. (1)] from the earlier measured values of the scattering law.

Another test of the pulsewidth calibration can be performed by using the depolarized measurements. As mentioned above, these were normalized in the same way as the polarized measurements but to an assumed scattering law of $S_D(\Theta) = \cos(\Theta)$.

In Fig. 8 there is plotted another series of graphs of the normalized depolarized backscatter for each of the pulsewidths that were used.

Since the pulsewidth dependence is a simple multiplicative calibration factor resulting from instrumental effects, the factor should be identical for both the depolarized and polarized data, insofar as the two receiver channels are identical. The receivers and signal-processing equipment were of identical design and also, since the two measurements were taken simultaneously, there would be no accidental distortions because of selection effects. In Fig. 9 there is plotted, again for each of the six pulsewidths, the ratio of polarized/depolarized backscatter deviation from the assumed mean. It is considered that the merging of the six graphs in Fig. 9 is strong evidence for the assumed pulsewidth dependence as well as for the relative accuracy of the measurements. The absolute accuracy in cross section per unit surface area is compromised by the somewhat uncertain transmitting gain of the radar antenna (about 2 to 3 dB uncertainty).

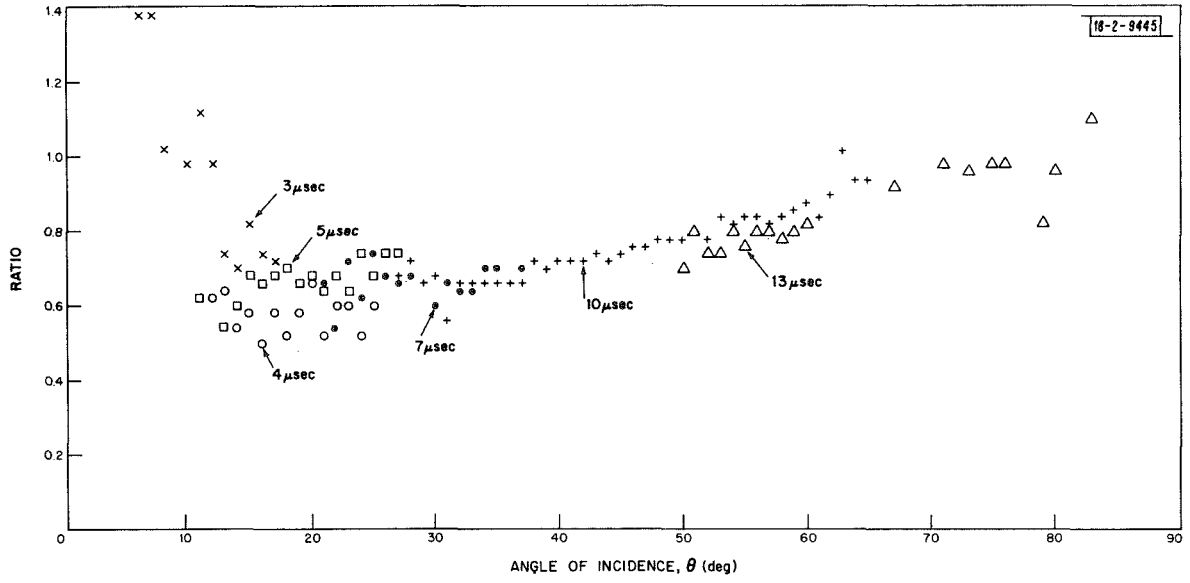

Fig. 9. Ratio of polarized/depolarized normalized backscatter, $P_p/P_D \cdot \cos(\theta)/S_p(\theta)$.

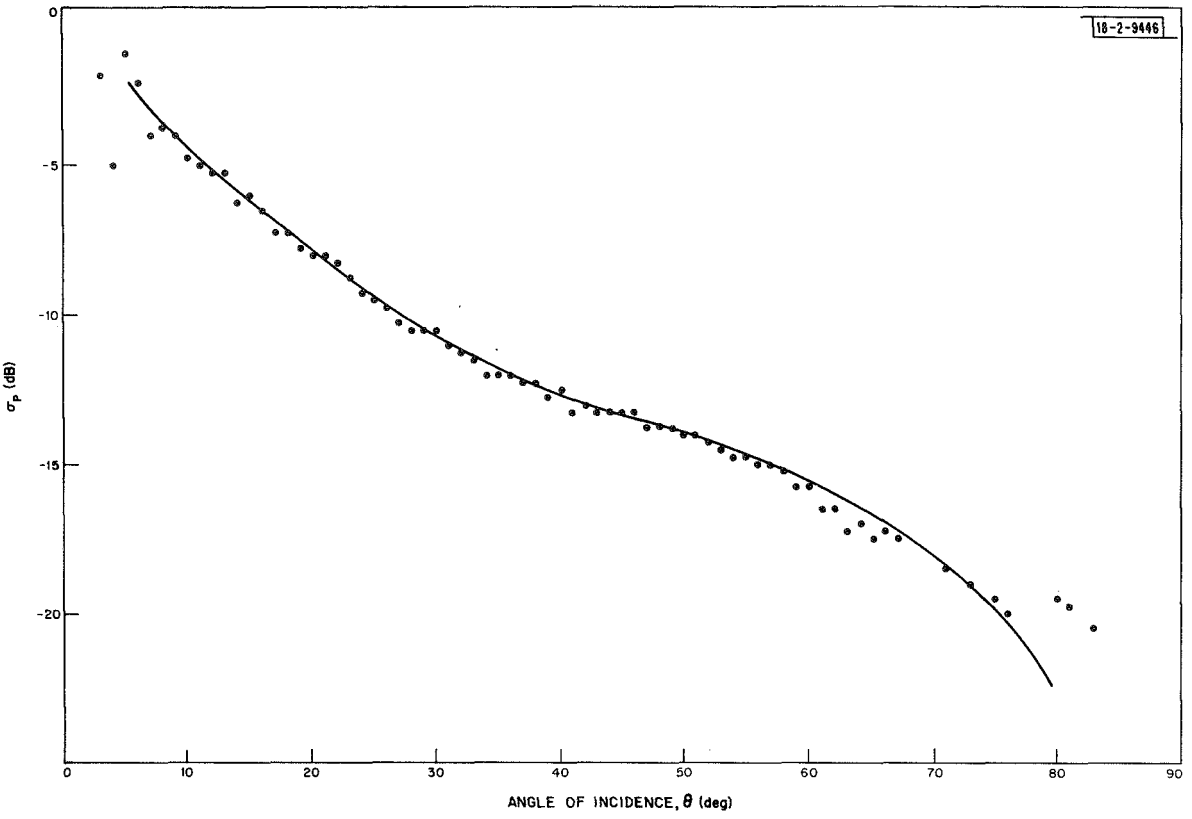

Fig. 10. 3.8-cm polarized scattering cross section per unit area, σ_p.

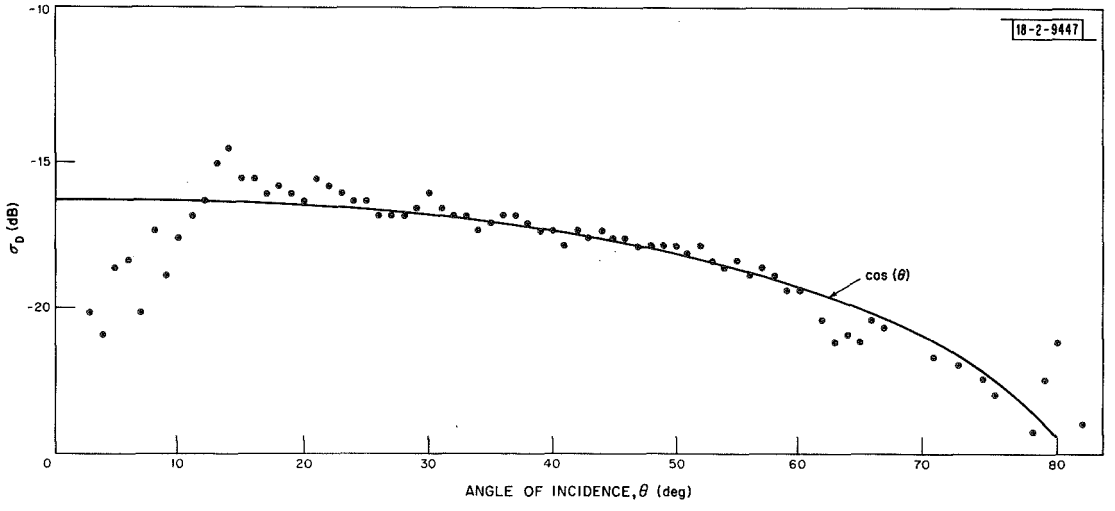

Fig. 11. 3.8-cm depolarized scattering cross section per unit area, σ_D.

The reason for the consistent droop at the ends of each of the pulsewidth graphs may be that only a few points are included at the extrema of each graph, and these have furthermore been measured near the edges of the antenna beam. The Gaussian beam correction is apparently insufficient and results in the observed distortion of the curves.

The graphs in Figs. 7, 8, and 9 represent an average of all the measurements in all the backscatter maps out through ZAC ring 8. In rings 9 and 10, the signals were so weak that the thermal radiation from the moon plus the receiver noise was a significant contribution to the total power. The thermal level was felt to be too dependent on antenna pointing for good quantitative measurements, and these data were omitted from the scattering law analysis.

The statistical variation in the averages is thus expected to be extremely small because of the large number of points included. On the other hand, the large-scale variation of the physical characteristics of the moon's surface adds an apparent randomizing factor to the average. In the preparation of the scattering curves, each data point corresponded to the average backscatter from an area about 80 × 80 km in size. The standard deviation of these points from the smooth scattering law of Fig. 5 is in fact about 30 percent, instead of the 2 percent expected from probability theory. This great spread in the backscatter suggests that an attempt should be made to form separate scattering laws and averages for the different large-scale geologic units on the surface. Such an attempt will be considered beyond the scope of the present report.

D. Summary

Several additional features of the scattering law measurements remain to be noted. These can best be observed in graphs of Figs. 10 and 11, which are the same polarized and depolarized data as in Figs. 7 and 8, but with the pulsewidth calibration factor applied and the result plotted as absolute backscatter in units of scattering area per unit surface area.

(1) The depolarization of radar echoes near the moon's limb is 0.33 ± 0.03, that is, the absolute ratio of depolarized/polarized signals averages 0.5 ± 0.05. This is essentially the same value as observed at 23-cm and 70-cm wavelengths.

(2) The most interesting feature from the point of view of the moon's surface structure is the significant decrease in the depolarized backscatter at angles less than 15° or 20°. No such effect has been observed at 70 and at 23 cm (see Fig. 6). Nevertheless, it may be present at longer wavelengths also but not be observable because of the much more serious cross-talk problem. There may be a suggestion of a downward trend in the 23-cm curve of Fig. 6 which is being swamped by a cross-talk peak.

In the next section we turn to a discussion of the physical causes of the various properties of the scattered signal.

III. RELATIONSHIP OF SURFACE PROPERTIES TO THE SCATTERING CHARACTERISTICS

Having shown how it is possible to produce high-resolution maps of reflectivity as a function of position on the moon for both circular polarizations, we must turn to the question of the physical significance of these numbers. As we shall see, the question of reflectivity is related both to the intrinsic electrical properties of the material and to the actual physical state of the material in terms of roughness, degree of compaction, distribution with depth, etc.

The radio-wave scattering properties of the moon are quite different from those at optical wavelengths. Whereas at optical wavelengths the backscattered light is relatively independent of the angle between the line of sight and the normal to the surface – giving the lunar disk the appearance of being uniformly bright – the most characteristic feature of the backscattered radio waves is the strong preference for reflection at normal incidence. This, in turn, causes a bright spot to appear at the center of the disk of the moon. Hence, it is immediately obvious that the lunar surface on the scale of a wavelength is much smoother on the centimeter and meter scales than it is on the scale of microns and tenths of microns.

If the moon were a perfectly smooth sphere, reflection would only occur from a very limited region near the subradar (i.e., sub-observer) point. A study of the moon by radar would then reveal little beyond the reflectivity at normal incidence in a limited region of the lunar surface. Fortunately, although the moon is relatively smooth on the scale of the wavelength of observation, there are large-scale deviations from the spherical shape in the form of mountains, craters, rilles, etc. The effect of these deviations from ideal spherical shape is to divide the central Fresnel zone (the contributing area when the surface is smooth) into a large number of "glints" which are distributed over an extended area over the disk of the moon. The distribution of "glints" as a function of distance from the subradar point may, as we shall see, give relatively precise information on the nature of the large-scale surface undulations in the regions near the center of the lunar disk.

As the observations show, signals are returned from the lunar surface from areas all the way to the limb. The strength, angular dependence, and depolarization properties of the returns at large angles of incidence are such that the most plausible explanation for these echoes is in terms of scattering from a rocklike structure of wavelength size or somewhat larger.

In the following section, we shall briefly review the quantitative background for drawing conclusions on the physical and electrical properties of the lunar surface material from the radar measurements of the mapping program. Some of the material in the section represents an updated and corrected version of certain parts of the Final Report, Volume 1, dated 31 August 1967.

A. The Reflectivity of the Smooth Surface

If the moon were a perfect sphere made of a lossy dielectric material, the radar cross section of the moon as a whole would be

$$\sigma_t = R_o \pi a^2 \quad , \tag{3}$$

where R_o is the power reflection coefficient at normal incidence and where a is the lunar radius. The modification required to compute the cross section of the moon for the case when large-scale undulations are present causing the central Fresnel zone to break up into glints is to multiply the above expression by $(1 + \alpha^2)$, where α is the rms slope of the surface undulations. Since the slope angle is typically on the order of 10°, the modification caused by the glints is rather minor.

The reflection coefficient R_o, in the case of a sharp boundary between the vacuum and the lossy dielectric, takes the form

$$R_o = \left| \frac{\sqrt{\epsilon - 1}}{\sqrt{\epsilon + 1}} \right|^2 \quad , \tag{4}$$

where ϵ is the complex relative dielectric constant of the lunar surface material. If conditions were this simple, the dielectric constant of the surface material could be determined directly from cross-section measurements.

There is now considerable evidence that the properties of the lunar soil change with depth from the Surveyor series of observations,[8] from wavelength dependence of the reflectivity of the moon,[9] and from certain observations of the thermal behavior of the lunar surface.[10] This variation with depth may take a number of different forms. One might suppose that there is a uniform layer with dielectric constant ϵ_1 and depth b overlying a semi-infinite homogeneous medium of dielectric constant ϵ_2. In the simple case where losses can be ignored, one obtains

$$R_o = \frac{\epsilon_1(\sqrt{\epsilon_2} - 1)^2 - (\epsilon_1 - 1)(\epsilon_2 - \epsilon_1)\sin^2(\sqrt{\epsilon_1}kb)}{\epsilon_1(\sqrt{\epsilon_2} + 1)^2 - (\epsilon_1 - 1)(\epsilon_2 - \epsilon_1)\sin^2(\sqrt{\epsilon_1}kb)} \quad , \tag{5}$$

where $k = 2\pi/\lambda$, λ being the free-space wavelength. It would be very unlikely that the depth b should remain constant over the whole surface of the moon – or from "glint" to "glint" – and the mean reflectivity could then be found from

$$R_o = \int_o^\infty R_o(b)\, p(b)\, db \quad , \tag{6}$$

where p(b) db is the probability of finding an upper-layer thickness between b and b + db. It will be appreciated that the mean reflectivity will depend strongly on the particular form of p(b). Only in the limiting cases of very small and very large layer depths is it possible to obtain simple expressions for the reflectivity, viz:

$$R_o = \left|\frac{\sqrt{\epsilon_2} - 1}{\sqrt{\epsilon_2} + 1}\right|^2 \qquad \text{(thin layer)} \quad , \tag{7}$$

$$R_o = 1 - \frac{4\sqrt{\epsilon_1\epsilon_2}}{(\sqrt{\epsilon_2} + 1)(\sqrt{\epsilon_2} + \sqrt{\epsilon_1})} \qquad \text{(thick layer)} \quad . \tag{8}$$

Thick and thin here refer to the layer thickness being greater or smaller than $\lambda/4\sqrt{\epsilon_1}$. Figure 12 shows the relationship of reflectivity to ϵ_1 and ϵ_2 for the thick surface layer case. We observe that various combinations of ϵ_1 and ϵ_2 can give rise to a large variation in reflectivity. Also, we should note that a wavelength dependence of the reflectivity is possible in this model as the transition between thin and thick layers takes place.

A gradual transition in electrical properties through the upper layer may be more realistic. One that can be handled mathematically has a dielectric constant which varies linearly with depth from a value of ϵ_1 at the top to ϵ_2 at the lower boundary. An example of the results is shown in Fig. 13. We notice that the reflection from the upper boundary becomes dominant when the transition layer depth is between 0.1 and 0.2 wavelengths.

Matveev[11] considered a possibly more realistic model where the refractive index was allowed to vary with depth z according to

$$n(z) = \{1 + w_o[1 - (1 - \beta)\, e^{-z/z_o}]\} \quad , \tag{9}$$

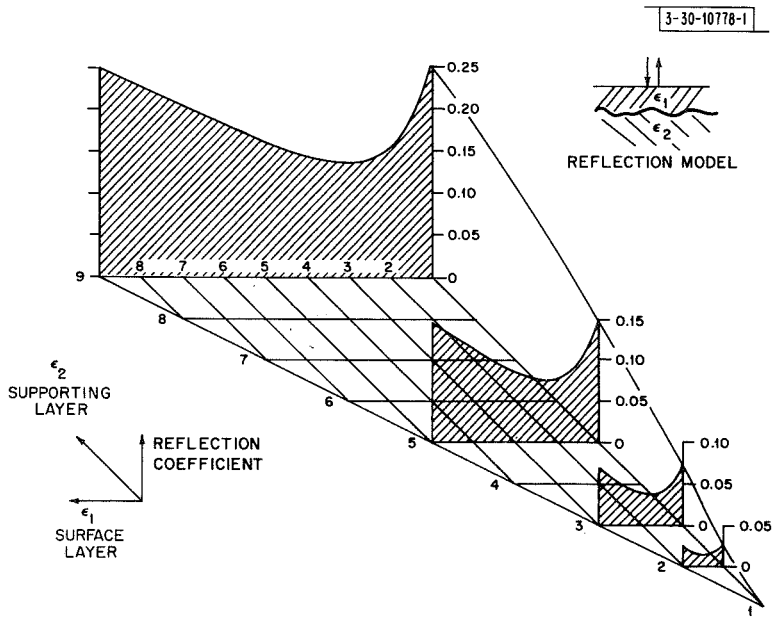

Fig. 12. Reflectivity of two-layer model of lunar surface (thick-layer case).

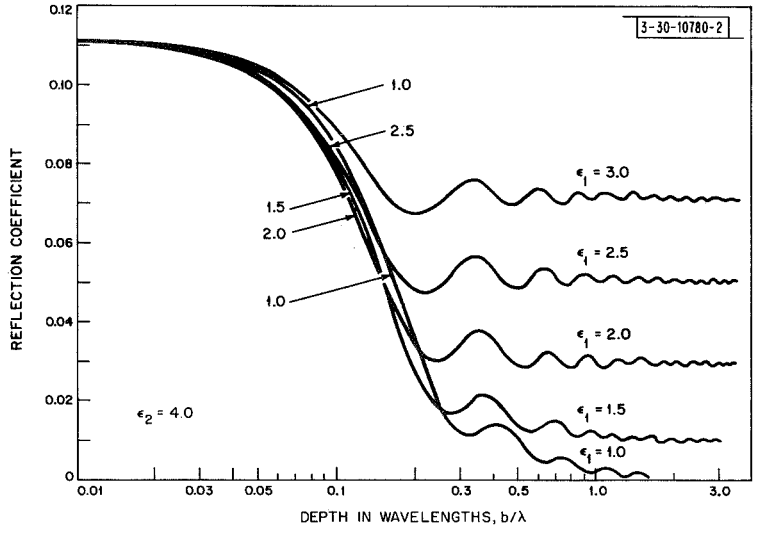

Fig. 13. Reflectivity of linearly-tapered-layer model of lunar surface (for $\epsilon_2 = 4.0$ at great depth).

where at the surface the dielectric constant $\epsilon_1 = (1 + \beta w_o)^2$ and at a great depth, $\epsilon_2 = (1 + w_o)^2$.

Figure 14 shows two examples of computational results. Again it can be seen that the reflection is determined entirely by the upper boundary when the transition layer is in excess of 0.2 wavelength.

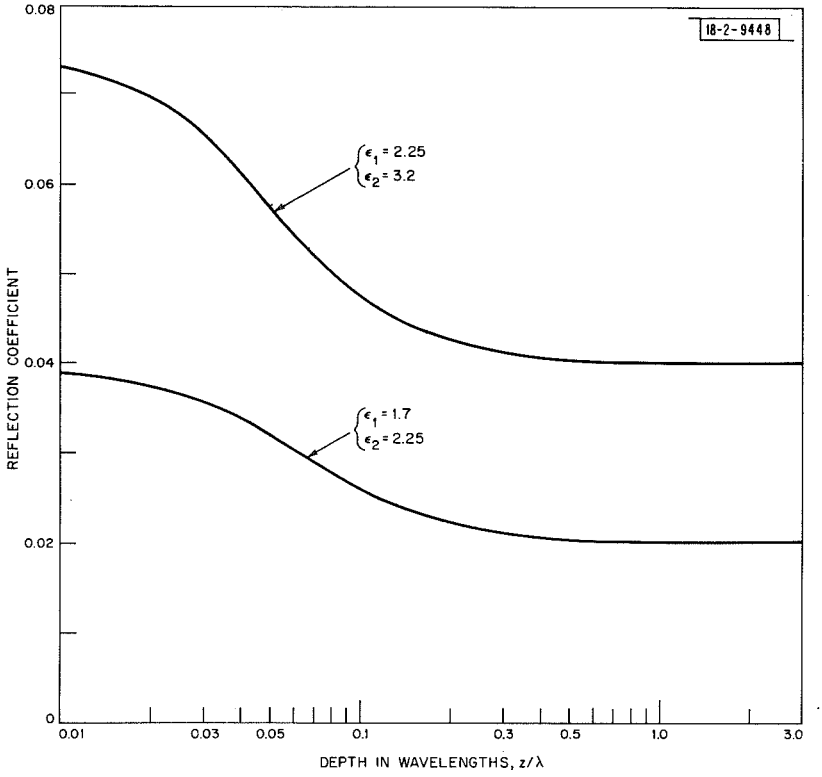

Fig. 14. Reflectivity of exponentially-tapered-layer model of lunar surface.

Further refinements have been introduced into the theory of reflection from a gradually changing boundary layer by Tikhonova and Troitskii.[12] In that theory, the density is assumed to vary with depth at first rapidly over a distance of a few centimeters, then slowly over a depth of several meters, after which the characteristics of solid rock are assumed to apply.

The wavelength dependence of the dielectric constant of the moon is shown in Fig. 15. The data have been obtained from, in addition to gross radar reflectivity, polarization of thermal microwave emission,[13] Brewster angle observations,[14] and spherical albedo measurements.[9] As can be seen, there is a somewhat vague, although probably significant, increase in the apparent dielectric constant with wavelength. Since this increase appears to continue beyond at least 10-meter wavelength, we may conclude from the curves of Figs. 13 and 14 that the tenuous surface layer must typically be thicker than some 200 cm. This conclusion, based on radio data, is consistent with results obtained by other means.[15,16]

The typical lunar ground consistent with the observations quoted and in accord with the theoretical considerations discussed in this section appears to have dielectric constant which increases with depth from some 1.5 to 1.7 at the top to at least 3.5 at a depth in excess of 200 cm

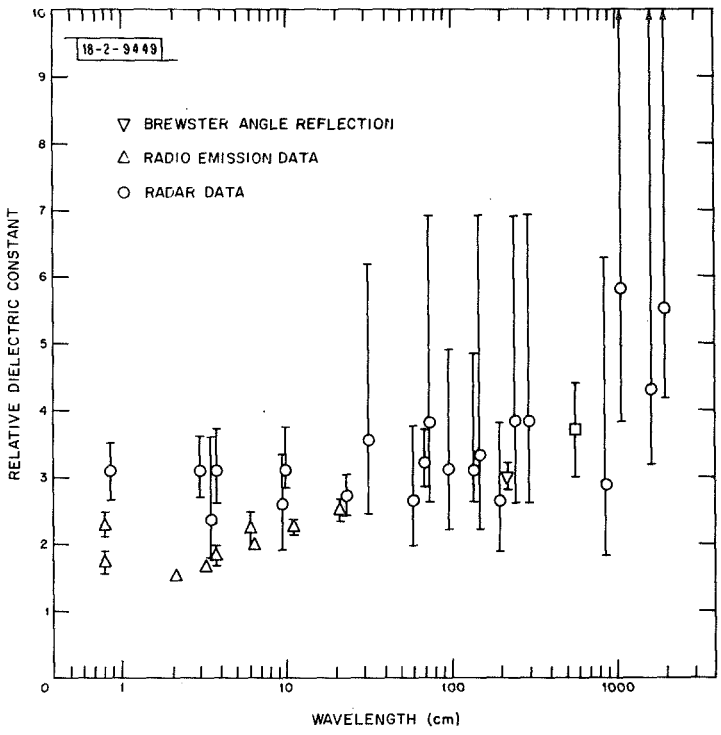

Fig. 15. Dielectric constant vs wavelength as calculated from gross reflectivity and other measurements.

or so. Tikhonova and Troitskii[12] propose a relationship between density and dielectric constant of the form:

$$\sqrt{\epsilon} = 1 + [0.5 + 0.045 \log(\lambda/3)] \cdot \zeta \quad , \tag{10}$$

where λ is expressed in meters and where ζ is in grams per cm^3, and conclude that the density of the lunar surface typically increases from 0.7 gr/cm^3 to 2.5 gr/cm^3 at a depth between 2 and 3 meters. The description of the maps to be presented must be regarded as deviations from this typical surface structure.

B. Effect of Surface Undulations

In the previous section we dealt with the reflection from a smooth moon which was allowed to possess variation in electrical properties with depth. In this section we shall be concerned with the returns arising as a result of deviations of the surface from perfectly spherical shape. Hence, we shall regard the surface in terms of the radial distance from the center of the moon as a function of latitude and longitude. In other words, we regard the deviation from spherical shape, z, as a function of Λ and φ.

A number of authors[17-19] have developed theories involving only the principles of geometric optics. In this approach, only surface elements oriented normal to the line of sight scatter back favorably and the reflection coefficient is simply taken to be the Fresnel reflection coefficient at normal incidence. Obviously, any one of the other forms of reflection coefficients discussed in the previous section could also be used.

Now suppose that in a given area in the vicinity of (Λ, φ), where the normal to the mean surface is $\vec{n}_o(\Lambda, \varphi)$, the probability per unit of mean surface area of having a surface normal $\vec{n}$ within a solid angle element $d(\vec{n})$ is given by

$$p\,[\vec{n} - \vec{n}_o(\Lambda, \varphi);\ \Lambda, \varphi]\ d(\vec{n}) \quad . \tag{11}$$

The latitude and longitude coordinates enter explicitly, not only through $\vec{n}_o$, since the statistical properties of the surface may vary from area to area. If the unit normal along the line of sight is $\vec{n}_r$, then the power returned per unit area from the vicinity of (Λ, φ) is given by

$$P(\Lambda, \varphi) = K \cdot R_o(\Lambda, \varphi) \cdot p\,[\vec{n}_r - \vec{n}_o(\Lambda, \varphi);\ \Lambda, \varphi]/\cos\varphi \quad , \tag{12}$$

where

$$\cos\varphi = \vec{n}_r \cdot \vec{n}_o,$$

$$K = \frac{1}{2} \cdot P_T \frac{G_T G_R \lambda^2}{64\pi^3 R^4},$$

P_T = transmitter power,

G_T, G_R = transmitter, receiver antenna gain at (Λ, φ),

λ = wavelength,

R = distance to area observed.

It is seen that the power returned is determined jointly by the slope statistics and by the reflectivity at normal incidence, as discussed in the previous section.

Other workers have chosen to treat the problem by employing diffraction theory. In this approach, the field at the receiver is connected to the fields over the target surface by means of Huygen's principle. The surface fields can only be established rigorously, however, by solving a complicated integral equation. For this reason it is assumed that the boundary fields may be established in terms of the tangent-plane approximation or in terms of a perturbation procedure originally due to Rayleigh. The former method, often referred to as the Kirckhoff method, is suitable for dealing with large-scale perturbations as long as the radius of curvature of the undulations is large compared with the wavelength. The latter approach is suitable only for dealing with surface perturbations which introduce shallow phase modulation in the wavefront. The shallow phase modulation case is apparently inadequate for the description of the returns from the moon. On the other hand, Kirckhoff's method is also unsatisfactory in dealing with the detailed behavior of the scattering, since certain reciprocity relations are violated as soon as one attempts to describe anything but the quasispecular return in this way. For details the reader is referred to a series of papers.[20-26] An excellent review was given by Barrick and Peake.[27]

In the diffraction theory approach, the surface is described by the statistics of the surface height deviation $z(\Lambda, \varphi)$. In nearly all the published papers, z is regarded as a Gaussian random variable and the second moment of z is described by a correlation function relating the height deviations at adjacent points on the surface:

$$\langle z_1, z_2 \rangle = \langle z^2 \rangle \rho(\Delta r) = h_o^2 \rho(\Delta r) \quad , \tag{13}$$

where Δr is the distance between the points 1 and 2 where z_1 and z_2 are measured. Both h_o and ρ must be regarded as slowly varying functions of position (Λ, φ). The backscattering per unit surface area becomes

$$P(\Lambda, \varphi) = K \cdot \frac{R_o(\Lambda, \varphi)}{\cos^2 \varphi} \int_o^\infty d(\Delta r) \cdot \Delta r J_o(2k \Delta r \sin \varphi)$$

$$\cdot \exp\{-4k^2 h_o^2 \cos^2 \varphi \, [1 - \rho(\Delta r)]\} \quad . \tag{14}$$

In this approach, where it has already been assumed that the phase modulation is deep and the statistics isotropic, the surface properties enter through the normal reflectivity $R_o(\Lambda, \varphi)$ and through $\langle z^2 \rangle$ and $\rho(\Delta r)$. In addition, the position of the mean surface with respect to the direction toward the radar plays an important role through the angle of incidence φ to the mean surface.

As long as $\rho(\Delta r)$ can be expanded about $\Delta r = 0$ in a power series

$$\rho(\Delta r) = 1 - \frac{\Delta r^2}{2} [-\rho''(0)] + \ldots \quad , \tag{15}$$

where

$$\rho''(0) = \frac{\partial^2 \rho}{\partial \Delta r^2} \quad \text{at} \quad \Delta r = 0 \quad ,$$

and as long as this is a good approximation to the correlation function within the range over which the exponential term is appreciably different from zero, we obtain for the power scattered per unit area at an angle φ

$$P_S(\Lambda, \varphi) = \frac{K}{\cos^4 \varphi \; h_o^2 \, [-\rho'']} \exp[-\tan^2 \varphi / 2h_o^2 (-\rho'')] \quad . \tag{16}$$

Assuming, for example, that the autocorrelation function is Gaussian,

$$\rho(\Delta r) = \exp[-\Delta r^2 / 2d_o^2] \quad ,$$

and hence that

$$\rho'' = -\frac{1}{d_o^2} \quad ,$$

the rms slope along any direction on the surface is

$$(t_x)_{rms} = (t_y)_{rms} = h_o / d_o \quad .$$

The "mean slope" or the mean value of the tangent of the angle between the normal to an arbitrary surface element and the normal to the mean surface becomes

$$\langle \tan \varphi \rangle = \sqrt{\frac{\pi}{2}} \frac{h_o}{d_o} \approx 1.25 \, h_o / d_o \quad .$$

The rms of the tangent of this angle becomes

$$\sqrt{\langle \tan^2 \varphi \rangle} = \sqrt{2} \, h_o / d_o \quad .$$

Let us next turn to cases where there is no simple relationship between true and apparent surface slopes. This occurs whenever the surface has a considerable amount of fine structure of a lateral scale not necessarily as small as the wavelength but of a vertical scale smaller than the wavelength of the exploring wave. This will bring about structural detail in the correlation function near the origin which will not appreciably influence the value of the integral [Eq. (14)] determining the backscattered power. This fine structure could, on the other hand, well be completely dominant in determining the true rms slope of the surface. In this situation, the slope distribution derived from our analysis can only apply to "apparent" slopes which differ from the true slopes as a result of the smoothing effect imposed by the finite electrical length of the incident waves. This smoothing scale, unfortunately, is a function of the angle of incidence of the radio waves on the surface. To see this, it is only necessary to refer again to the integral [Eq. (14)] giving the backscattering power per unit area as a function of angle of incidence φ. When ρ is close to zero, the integral is determined primarily by a range of Δr extending from 0 to Δr_e, where Δr_e is the solution of the equation

$$4k^2 h_o^2 \cos^2 \varphi \, [1 - \rho(\Delta r_e)] = 1 \quad . \tag{17}$$

For somewhat larger angles of incidence φ, it will be the Bessel function that limits the range of Δr over which significant contributions to the integral are obtained. The range of Δr as determined by the "width" of the Bessel function extends from 0 to Δr_B, and it is given, at least in order of magnitude, by

$$\Delta r_B = \frac{1}{k \sin \varphi} \quad . \tag{18}$$

To relate the range of scales on the surface to the range of separations Δr, we can expand $\rho(\Delta r)$ into a power spectrum

$$\rho(\Delta r) = \frac{1}{2\pi} \int_o^\infty \kappa d\kappa \cdot F(\kappa) \, J_o(\Delta r \cdot \kappa) \quad . \tag{19}$$

In writing Eq. (19), we have assumed that the surface deviations can be regarded as a sum of many waves of different frequency κ. The function $F(\kappa)$ is then a measure of the amplitude of each wave. For most random rough surfaces, the amplitude spectrum $F(\kappa)$ usually decreases monotonically with increasing frequency. As examples, consider the Gaussian autocorrelation function for which we obtain

$$F(\kappa) = 2\pi d_o^2 \exp[-\kappa^2 d_o^2/2] \quad , \tag{20}$$

and for the exponential autocorrelation function often used,[23] i.e.,

$$\rho(\Delta r) = \exp[-\Delta r/d_1] \quad , \tag{21}$$

we obtain

$$F(\kappa) = 2\pi d_1^{-1} (d_1^{-2} + \kappa^2)^{-3/2} \quad . \tag{22}$$

Since the fine structure in the correlation function in the range of Δr either from 0 to Δr_e [Eq. (17)] or from 0 to Δr_B [Eq. (18)] cannot appreciably affect the integral in Eq. (14), we conclude that an approximation to the received power is obtained by "filtering" out the high-frequency components in $F(\kappa)$ by writing

$$\rho_e(\Delta r) = \frac{B}{2\pi}\int_o^{\kappa_M} \kappa d\kappa F(\kappa)\, J_o(\Delta r \cdot \kappa) \quad , \tag{23}$$

where B is a normalizing constant and

$$\kappa_M = \begin{cases} 1/\Delta r_e \quad , & \Delta r_B > \Delta r_e \quad , \\ 1/\Delta r_B \quad , & \Delta r_B < \Delta r_e \quad . \end{cases} \tag{24}$$

This approximation can only be regarded as somewhat crude. A filtering function should have been applied to Eq. (28), and this filtering function would not necessarily have the rectangular shape there implied. For this reason, the procedure discussed serves only to illustrate the gradual decrease in the scale of the effective irregularities with increasing angle of incidence. Also, because of the truncation, h_o^2 must be adjusted somewhat to be an effective h_e^2 through

$$h_e^2 = h_o^2 \int_o^{\kappa_M} \kappa d\kappa F(\kappa) \Big/ \int_o^{\infty} \kappa d\kappa F(\kappa) = \frac{h_o^2}{B} \quad . \tag{25}$$

For a Gaussian autocorrelation function, one obtains

$$\kappa_M = \begin{cases} \dfrac{\sqrt{2_2}\, kh_o \cos\varphi}{d_o} & \text{when } \tan\varphi < \sqrt{2} \cdot \dfrac{h_o}{d_o} \quad , \\ k \cdot \sin\varphi & \text{when } \tan\varphi > \sqrt{2} \cdot \dfrac{h_o}{d_o} \quad . \end{cases} \tag{26}$$

As long as κ_M is large in comparison with $1/d_o$, there will be little effect of the truncation, since it makes little difference whether the integration in Eq. (23) is carried to infinity or to κ_M under these circumstances. This condition on κ_M is closely related to the assumption of a "deep" phase screen (i.e., $kh_o > 1$) with gentle slopes (i.e., $h_o/d_o < 1$). For the Gaussian autocorrelation function, it is therefore seen that the same range of scales will contribute to the scattered power at all angles of incidence.

In certain situations, e.g., the exponential autocorrelation function, the power spectrum $F(\kappa)$ decays sufficiently slowly with scale frequency κ that the effective autocorrelation function $\rho_e(\Delta r)$ appreciably changes form with κ_M. Since κ_M is increasing with the angle of incidence φ, the smallest scale of those components responsible for backscattering is decreasing with increasing angles of incidence. This in turn brings about an increase in the effective slope with increasing angles of incidence. When this effect is appreciable, the interpretation of the backscattered power as a function of angle of incidence in terms of a geometric optics model[19] is of doubtful value.

The effective slope of the filtered version of the surface may be defined in analogy with the Gaussian autocorrelation case as follows:

$$\frac{h_e^2}{d_{eo}^2} = -h_e^2 \rho_e''(0) = \frac{h_o^2}{4\pi}\int_o^{\kappa_M} \kappa^3 F(\kappa)\, d\kappa \quad . \tag{27}$$

The lunar data will not fit a simple model involving the Gaussian autocorrelation function. Instead, a reasonably good fit over angles of incidence smaller than 15° is obtained by using the exponential correlation function. In this case, one obtains for the backscattering cross section per unit surface area

$$\sigma = \frac{CR_o}{2\cos^6\varphi}\left(1 + C\,\frac{\tan^2\varphi}{\cos^2\varphi}\right)^{-3/2} \quad , \tag{28}$$

where

$$C = (d_1\lambda/4\pi h_o^2)^2 \quad .$$

In the case of data obtained at 68- and 23-cm wavelength, the mean scattering law follows very closely a relationship such as (26) for small angles of incidence with values of C of 95 and 65, respectively, and with normal reflectivities R_o of 0.0697 and 0.0648, respectively (see Fig. 5). At 3.8 cm, the agreement with (26) is relatively poor. The best fit occurs for C = 40 and R_o = 0.05. Concentrating for the moment on the 23- and the 68-cm data, assuming deep phase modulation, we obtain

$$\Delta r_e = \lambda\sqrt{C}/(4\pi\cos^2\varphi) \quad . \tag{29}$$

Hence, even for near normal incidence, the scales of importance extend down to wavelength size. The effective slope now becomes approximately

$$\frac{h_e^2}{d_{eo}^2} \approx \frac{\cos^2\varphi}{2C(\kappa_M)} \quad . \tag{30}$$

This appears to imply that the angles corresponding to the rms slopes at the scale of 68 and 23 cm, respectively, are 6° and 7°. These values are noticeably lower than the 10° to 12° that one would tend to derive on the basis of geometrical optics (e.g., Ref. 19). The discrepancy only reflects the difficulty of assigning a slope parameter to the lunar surface structure.

Marcus[28] has recently developed a theory of scattering on the basis of a Cauchy distribution of surface slopes and has come to the conclusion that a surface slope of 5.7° is characteristic of the lunar surface on the scale of one meter.

C. Diffuse and Depolarized Scattering

We now come to the potentially most interesting and physically most significant part of the return – that which cannot be explained as a specular return or "glint." The so-called diffuse part of the return is characterized by a moderately fast dependence on angle of incidence, such as $\cos\varphi$ or, perhaps, $\cos^{3/2}(\varphi)$. It is also characteristic of this component that there is a very considerable depolarization. For circularly polarized illumination, the depolarized component may be only 3 to 4 dB weaker than the polarized component, whereas for linearly polarized illumination the depolarized component may be some 5 to 6 dB weaker than the polarized component. It should be pointed out here, since it may be significant from a physical point of view, that the ratio polarized circular/depolarized circular approaches 3 dB at $\varphi \to 90$ for wavelengths of 70, 23, and, from the present measurements, 3.8 cm.

Several authors have attempted to explain the diffuse and the depolarized components by Kirckhoff theory.[29,30] As explained above, this theory is unsuitable for this purpose, since the

boundary conditions are nonreciprocal for the nonspecular part of the return. As an example of the difficulties which may arise with this type of explanation, the reference to Beckmann[29] is typical. Beckmann finds maximum depolarization when the angle β between the E-vector and the plane of incidence is 45° and minimum when β is 0° or 90°. Observations carried out by Hagfors[1] at 23-cm wavelength, however, show that depolarization is minimum when $\beta = 0°$ and maximum when $\beta = 90°$. This example, the assumptions underlying the theory, and other indications lead us to reject the Kirckhoff theory as an explanation for anything but the quasispecular or "glint" part of the echo. For further discussion the reader is referred to Kodis[31] or to Barrick.[32]

Some attempts have been made to merge the Kirckhoff method with Rayleigh's perturbation method.[33] This, at least on the surface, looks like a potentially useful approach. However, the results available from this technique are at present not sufficiently complete for a thorough evaluation and have besides been severely criticized on the theoretical grounds.[34]

A reasonably consistent explanation of the diffuse and the depolarized return may be obtained from a naive model suggested by Hagfors[1] from studies of the depolarizing properties of the moon at 23-cm wavelength. In this model the diffuse return is considered to be the result of scattering from discrete objects such as rocks strewn over the surface or possibly buried inside the lunar regolith. Surveyor photographs are certainly also suggestive of this rock-model.

In what follows, we shall attempt to arrive at some plausible consequences of this proposition in the form of wavelength dependence, angular dependence, and reflectivity. Consider first the effect of the surface rocks on the reflectivity.

When all the rocks are deposited on the surface, an approximate value of the reflectivity can be obtained as follows. The backscattering cross section of a rock of diameter a is given by

$$\sigma_R = \pi \frac{a^2}{4} \times g \times \bar{R} \quad , \tag{31}$$

where g is the gain function in the backscatter direction, and where $\bar{R}$ is the effective albedo. Both the backscatter gain function and the albedo $\bar{R}$ are functions of wavelength of observation. Now, let the number of scatterers per unit surface area with diameter between a and a + da be n(a) da. The total contribution to the cross-section per unit area from exposed rocks of size a between a and a + da becomes

$$\sigma_a = \frac{\pi}{4} a^2 g \bar{R} n(a)\, da \tag{32}$$

The total cross section per unit area due to the rocks hence becomes

$$\sigma = \frac{\pi}{4} \int_0^\infty a^2 n(a)\, g(a,\lambda)\, \bar{R}(a,\lambda)\, da \quad . \tag{33}$$

These considerations must be regarded as very crude because of the fact that the rocks are resting on or in a dielectric surface which at least at grazing angles of incidence is quite reflective. One might, nevertheless, obtain an order of magnitude estimate of the cross section if the gain function $g(a,\lambda)$ and the albedo $\bar{R}(a,\lambda)$ were known accurately. In the first calculations of this type by Hagfors,[1] the cross section of an individual rock was taken to be equal to the geometrical cross section times the reflectivity of the moon as a whole for $a > \lambda$ and zero when $a < \lambda$. This procedure has been criticized by Thompson, et al.,[5] who point out that isolated dielectric spheres

can be much more reflective than metallic spheres of the same diameter. Extensive calculations have been carried out by many authors on this problem, e.g., Atlas, et al.[35] These authors find that, for a refraction index of 1.61 (or $\epsilon = 2.6$) and an imaginary part of 0.0025, the cross section increases to a maximum on the order of ten times the geometrical cross section for $k_o \cdot a \approx 4$ and thereafter declines gradually. Typical lunar rock will have a higher dielectric constant and also a higher loss tangent. The higher dielectric constant may be inferred from the cross-section data quoted above. The higher losses may be deduced from radiometric observations of thermal emission from the moon (see Linsky[36] or Troitskii[37]). The skin depth of the lunar regolith is found to be approximately 20 λ. The skin depth in rocks will therefore probably be in the range of 5 to 10 λ if we assume the regolith to be rock-powder with slightly more than 50 percent void. The cross section of a lossy dielectric sphere will begin to approach the geometric optics cross section when π a is larger than the skin depth because many of the modes responsible for the large cross section will then be heavily damped. For the backscattering cross section, one may assume that

$$\sigma_R = \begin{cases} 0 & \text{when } \pi a < \lambda \quad , \\ 10\ \frac{\pi}{4}\ a^2 & \text{when } \lambda < \pi a < 10\lambda \quad , \\ 0.1\ \frac{\pi}{4}\ a^2 & \text{when } \pi a > 10\lambda \end{cases} \tag{34}$$

This is probably correct at least to the nearest order of magnitude. For the cross section per unit surface area one obtains

$$\sigma = \frac{\pi}{4}\left[10 \int_{\lambda/\pi}^{10\lambda/\pi} a^2 n(a)\, da + 0.1 \int_{10\lambda/\pi}^{\infty} a^2 n(a)\, da\right] \quad . \tag{35}$$

The only information available at present on the rock distribution is that obtained from the various Surveyor experiments. Table III, taken from "Surveyor, Program Results, NASA SP-184, 1969," summarizes the results.

TABLE III

SIZE-FREQUENCY DISTRIBUTIONS OF SURFACE PARTICLES AT THE SURVEYOR LANDING SITES

(Constants and exponents of functions of the form $N = Ka^{\gamma}$, 1 millimeter $\leqslant a \leqslant K^{-1/2}$ fitted to observed distributions.)

Landing Site	K, mm^{γ} 100 m^2*	γ*
Surveyor I	5.0×10^5	−2.16
Surveyor III	3.3×10^6	−2.56
Surveyor V	1.25×10^6	−2.65
Surveyor VI	1.91×10^6	−2.51
Surveyor VII	7.9×10^5	−1.82

* $N = Ka^{\gamma}$, 1 mm $\leqslant a \leqslant K^{-1/\gamma}$, where N is the cumulative number of particles with diameter equal to, or larger than, a per 100 m^2, and a is the diameter of particles in millimeters.

TABLE IV

DISTRIBUTION n(a) AND CUMULATIVE DISTRIBUTION N(a) FOR LUNAR ROCKS – UNITS OF m^{-2}, a = DIAMETER IN m

Landing Site	N(a)	n(a)
Surveyor I	$2.34 \times 10^{-3} \times a^{-2.11}$	$4.95 \times 10^{-3} \times a^{-3.11}$
Surveyor III	$0.69 \times 10^{-3} \times a^{-2.56}$	$1.77 \times 10^{-3} \times a^{-3.56}$
Surveyor V	$0.14 \times 10^{-3} \times a^{-2.65}$	$0.37 \times 10^{-3} \times a^{-3.65}$
Surveyor VI	$0.56 \times 10^{-3} \times a^{-2.51}$	$1.41 \times 10^{-3} \times a^{-3.51}$
Surveyor VII	$27.4 \times 10^{-3} \times a^{-1.82}$	$49.7 \times 10^{-3} \times a^{-2.82}$

The cumulative distribution and the density converted to rocks per m^2 and with diameter measured in m are given in Table IV. With a distribution of the form indicated in Table IV, i.e., $n(a) = C \cdot a^{-s}$, one obtains for the cross section per unit area caused by rocks alone

$$\sigma = \frac{\pi \cdot C}{4(s-3)} \left(\frac{\lambda}{\pi}\right)^{3-s} (10 + 10^{2-s} - 10^{4-s}) \quad , \tag{36}$$

provided $s > 3$ which is the case for all the sites with the exception of that of Surveyor VII. Let us digress at this point to deduce the wavelength dependence for the mean scattering from the moon. It was previously found from observations[1] that

$$\sigma \sim \lambda^{-0.32} \qquad 3.8 < \lambda < 23\,\text{cm} \quad ,$$

$$\sigma \sim \lambda^{-0.26} \qquad 23 < \lambda < 68\,\text{cm} \quad .$$

This would imply a value of s of 2.68 in the former case and 2.74 in the latter case. Considering that the Surveyor rock-count only included specimens up to about 50-cm diameter, one should focus attention primarily on the former s-value, 2.68. We see that the wavelength dependence is very close to what is to be expected from the Surveyor V result, and that it is reasonably close to what one might expect of the other landing sites, with the exception of the Surveyor VII site. The Surveyor VII site has a peculiar frequency-size distribution. Large fragments are so frequent that the integrals do not converge, indicating that the distribution function cannot be extrapolated to very large sized rocks. In any case, if the scattering by rocks hypothesis is to be trusted, one would expect the wavelength dependence of the return in the Surveyor VII area (near Tycho) to be quite different from what it is elsewhere on the moon. Pettengill and Thompson[4] have studied the Tycho region in great detail and have found an average relative enchancement in scattering at 68 cm of 5.0 ± 1.0, whereas the relative enchancement at 3.8 cm is only about 2.0 ± 0.3. Since the scattering per unit area for the mean surface at the angle of incidence of Tycho should be 2.4 times stronger at 3.8 cm than at 68 cm, it follows that the scattering cross section per unit area in the Tycho region is practically waveleng h-independent. This is consistent with the extraordinary distribution function observed at the Surveyor VII site and hence provides additional evidence in favor of the rock-fragment scattering hypothesis.

We next have to consider the question of whether the total scattering cross section observed is compatible with the rock-counts of the Surveyor experiments. It must be kept in mind that this comparison is much less reliable than the comparison of wavelength-dependence with rock-count distribution since the backscattering cross section of each rock is highly uncertain.

TABLE V

COMPARISON OF SCATTERING CROSS SECTION PER UNIT AREA OBSERVED AND ESTIMATED (in dB)

Landing Site	φ (deg)	Computed Rock Reflectivity	Observed, Relative to Mean Law	Total Power Scattered
Surveyor I	45	−8.4	−3.5	−19.3
Surveyor III	29	−6.7	−0.2	−12.5
Surveyor V	27	−12.1	−3.0	−14.8
Surveyor VI	~0	−8.6	–	–

Agreement to within an order of magnitude is all we may expect. The cross section per unit area to be expected from the Surveyor observations, except Surveyor VII, are given in Table V as deduced from Eq. (36).

Table V appears to indicate that the surface rocks are adequately abundant to account for all the scattering at the Surveyor landing sites. Note that no comparison could be made with Surveyor VI because of the proximity of this landing site to the center of the moon where $\varphi = 0°$. Note also that the entries in the last column include a certain amount of quasispecular return from the undulating surface – particularly of Surveyor III and V landing sites. There is some indication from the limited data that the rock reflectivity calculations may tend to order the reflecting areas correctly. The absolute magnitude of the calculated cross sections are too large by a factor of about 10, indicating that the model of freely suspended spheres used in the calculations drastically overestimates the effective reflectivity of the rocks. It also fails to account for an angular dependence. It is probable that this is related to the rocks being in the vicinity of the surface or even partly buried in the surface. The mathematical problem of estimating the reflectivity of the rocks in the presence of the surface has not to our knowledge been solved and could well be subjected to both experimental and theoretical study.

In view of the large uncertainty involved in the computation of the backscattering from surface rocks, we shall also discuss the possibility that all or part of the scattering takes place from rocks buried in the lunar regolith as first suggested by Hagfors, et al.,[38] on the basis of 23-cm polarization observations. Although our calculations so far seem to indicate that quite adequate power may be returned by surface rocks alone, we shall see that some of the features of the received signal may be explained quantitatively more easily in terms of buried scatterers.

Suppose a power density of unity is incident on the surface at an angle of incidence of φ. The power density immediately inside the regolith then is

$$S_i = T \cos \varphi_t / \cos \varphi \quad , \tag{37}$$

where φ_t is the angle of incidence below the boundary, and where T is the transmission coefficient. The power density at a depth of z becomes

$$S(z; \varphi_t) = (T \cos \varphi_t / \cos \varphi) \exp[-z/d \cos \varphi_t] \quad , \tag{38}$$

where d is the penetration depth in the regolith. The power scattered in a solid angle $\Delta\Omega_t$ inside the regolith when the cross section is σ_R becomes

$$P_t = (T \cos \varphi_t / \cos \varphi) \exp[-z/d \cos \varphi_t] \frac{\sigma_R}{4\pi} \Delta\Omega_t \tag{39}$$

For a volume distribution of scatterers of ρ, the scattered power within a solid angle $\Delta\Omega_i$ centered on the backscattering direction on the outside of the regolith (corresponding to $\Delta\Omega_t$ inside the regolith) and originating in a volume element A · dz becomes

$$P_{r,\Delta V} = T^2 \cdot \exp[-2z/d \cos\varphi_t] \frac{\sigma_R}{4\pi} \rho A \cdot dz \Delta\Omega_t \quad . \tag{40}$$

The cross section per unit surface area then becomes

$$\sigma = T^2 \cdot \sigma_R \cdot \rho \frac{\Delta\Omega_t}{\Delta\Omega_i} \int_0^\infty \exp[-2z/d \cos\varphi_t)\ dz$$

$$= T^2\sigma_R \cdot \rho \frac{1}{2} \frac{1}{\epsilon} \frac{\cos\varphi}{\cos\varphi_t} d \cdot \cos\varphi_t$$

$$= T^2 \cdot \sigma_R \cdot \rho \frac{1}{2} \frac{1}{\epsilon} d \cdot \cos\varphi \quad . \tag{41}$$

An angular dependence arises through the product $T^2 \cos\varphi$ in this expression. In addition, it is not inconceivable that the angle of incidence may be involved in σ_R. The penetration depth d is approximately proportional to wavelength λ. The density of rocks ρ is a volume distribution similar to the surface distribution n(a) introduced above in this discussion. If the surface distribution n(a) is just a manifestation of a volume distribution g(a), one might argue that only rocks having their center within $\pm a/2$ of the boundary will be counted in the surface distribution. This means that (see also Rosiwal[39])

$$\rho(a) \sim a^{-1} n(a) \quad . \tag{42}$$

The frequency dependence of the backscattering would therefore be close to what was derived for the surface distributions above, provided that the transmission coefficient T is not frequency-dependent to any appreciable degree. Since the cross section σ_R is as uncertain here as in the case of the surface scattering calculations, we shall not pursue the calculation of the scattering from buried rocks in any further detail.

Next, let us turn to a brief discussion of the depolarized component, i.e., that component which would be absent if the scatterer were an ideal metallic mirror-like reflector. Depolarization of a circularly polarized transmitted wave may be thought of as arising in at least two different ways. There may be a systematic difference between two orthogonally polarized linear scattering components. As an example, consider the case where one linearly polarized scattering component is zero and the orthogonal one is different from zero. In such a situation, the two orthogonal circularly polarized components returned, as a result of a circularly polarized illumination, would be of equal strength. An alternative cause of the depolarization of circularly polarized waves might be a general depolarization of the orthogonal linearly polarized components such that there is a "spillover" from one into the other which cannot be characterized as merely a rotation. A systematic investigation at 23 cm (Ref. 1) has shown that, although the former effect is present, it is the latter which is the primary cause of the circular depolarization. Presumably, the same applies in the case of the 3.8-cm returns.

We therefore visualize that the depolarized return is caused by discrete scatterers which are able to turn an effective plane of polarization nearly at random. As a mental crutch, one might imagine the scatterers to be linear dipoles oriented at random. Clearly, this is incompatible with the freely suspended spherical dielectric objects discussed above. However, it

could well be compatible with elongated objects oriented at random and either being exposed or buried in the surface layer.

We should realize at this point that the quasispecular return caused by large-scale surface undulations as discussed in the previous section must be absent in the depolarized part of the return. For this reason, the depolarized return is relatively insensitive to slopes when compared with the polarized return, at least for angles of incidence smaller than 20° to 30°. In other words, whereas the polarized return resembles the optical pictures obtained under low-angle illumination, the depolarized return in the central part of the lunar disk has more of the character of the optical picture at full moon (Fig. 16).

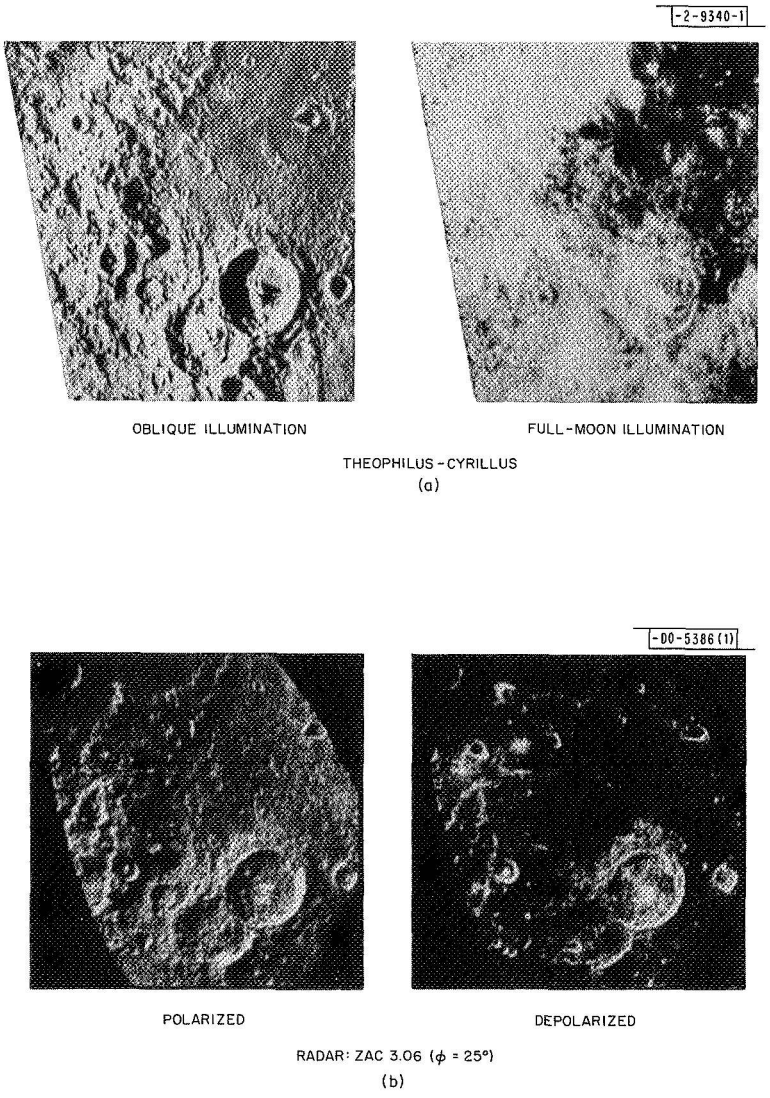

Fig. 16. Comparison of radar and optical appearance of lunar surface at small radar angle of incidence.

So far, we have made a case for regarding the diffuse and the depolarized part of the lunar radar echoes as a single scattering from a distribution of discrete objects. We have implicitly assumed that multiple scattering phenomena are unimportant. The only justifications for this assumption lie in the relatively low cross section of the individual scatterers and in the low density of scatterers.

It has often been claimed that there may be a very close relationship between infrared hot-spots[6] as observed during lunar eclipses and the radar returns, particularly the depolarized ones. Since the radar returns at oblique incidence – the depolarized ones in particular – are almost certainly caused by an increase in the number of surface or subsurface rocks, one might think that the hot-spots could be caused by the same physical situation. Many mechanisms have been proposed as explanations of hot-spots. It has been suggested that a hot-spot is caused by emissivity enhancement in certain areas. It has been shown, however, by Salisbury and Hunt[40] that in order to produce temperature differentials of some tens of degrees Kelvin, the hot-spot must possess an emissivity-deviation of a factor of two or so. Emissivity differences as large as this are inconsistent with emissivity variations observed in terrestrial rocks. Differences in infrared transparency may also produce the observed variation in the thermal response.[41] This mechanism is also thought to be an unlikely explanation, since excessively large transparency differences would be required.[10] Bare rock or a rock substratum covered by a very thin layer of dust has also been suggested as an explanation of the hot-spots.[42] Unfragmented rock, however, would generally produce too large temperature enhancements. Internal heat sources could produce hot-spots during eclipses, but hot-spots should then also be very prominent during the lunar nighttime, which they are not. A change in the microstructure of the regolith toward larger particles could also provide an explanation for the hot-spots.[43] It has been shown that a three- to fourfold increase in effective particle size could produce temperature differentials of 25 percent during an eclipse. Calculations by Roelof[44] have shown that a large rock on the surface might cool sufficiently slowly to contribute significantly to the slower cooling rate of the infrared hot-spots. This latter hot-spot model has led to the expectation that there is an intimate relationship between hot-spots and radar bright regions. Our investigations have suggested, however, that the relationship is more indirect than originally anticipated. Hot-spot temperature contours have a tendency to increase monotonically from outside the crater toward the central peak. The radar contours, however, often maximize along the crater rims and at the central peak, but show a dark crater floor. This difference is evident even in those craters that are large enough to be well-resolved by the infrared measurements. For this reason, it may be that some or all of the infrared hot-spots are controlled by the small-scale particle distribution in the regolith rather than by the larger-scale structure "visible" to the radar.

It may be appreciated that currently available ideas of the scattering mechanism in the diffuse tail of the radar return are rather vague and incomplete. It seems fairly certain that the depolarized, as well as the diffuse part of the polarized return, originates from scattering by a rock-like structure and that the strength of this part of the echo is related to the density of surface rocks. There also appears to be a significant relationship between the wavelength dependence of the diffuse component and the size-count frequency distribution of lunar rocks.

The angular variation of the scattering and particularly the low value in the depolarized return discovered by this study near 0° angle of incidence are not yet adequately explained. The $\cos \varphi$ dependence near $\varphi = 90°$ of the depolarized return could be caused by omnidirectional reradiation but need not necessarily be.

In the following section, as an introduction to the presentation of the data, we shall summarize the results of importance for arriving of the physical properties of the surface. The descriptions that then follow are based on interpretations of the data that appear reasonable in the light of present understanding of the scattering process. It is suggested, however, that the reader refer back to the present section to assess for himself the confidence level which can be assigned to the interpretations given.

IV. ORGANIZATION OF THE DATA AND INTERPRETATION OF SELECTED MAPS

Let us briefly summarize what we have learned from our discussion of scattering mechanisms as an introduction to a presentation of our data and an interpretation of some selected data.

When the angle of incidence is less than approximately 25°, the polarized component is dominated by the quasispecular "glint"-like component. The strength of the polarized echo in a particular area depends on the surface slope statistics as well as on the effective reflectivity at normal incidence. The strength of the depolarized return, on the other hand, even in this region should be strongly sensitive to the presence of exposed and buried rocks, and quite insensitive to the effect of local tilts.

For angles of incidence greater than 25° or so, the quasispecular component is no longer the dominant influence in the polarized component. Rather, the presence of surface rocks of sufficient size and number density, or possibly the presence of small-scale surface "ripple," may account for the major fraction of the return. The depolarized component is in all likelihood practically entirely determined by the presence of surface rocks. We should also observe that the wavelength dependence of the scattering, if it is available through comparison of our data with those of others, such as Arecibo at 70-cm wavelength, may give an indication of the rock-size distribution of the area under consideration.

Let us now turn to the organization of the observational material.

A. The Radar Atlas

The data are provided quantitatively to NASA workers on digital magnetic tapes, and instructions for their use are included. For visual inspection and selection of interesting areas for study, the backscatter data are also presented in the form of gray-scale photographs. For the data in each ZAC-map, a maximum value of backscatter S_{max} was chosen, and the interval from 0 to S_{max} was divided into 20 equal intervals. The photographs comprise 20 equally spaced exposure levels from (0 = black) to (20 = white) for lunar surface elements with backscatter within the corresponding intervals. Peaks above S_{max} were clipped to exposure level 20. In practice, the logarithmic response of the photographic process causes the upper four or five levels to be essentially undistinguishable. The level of S_{max} was chosen for a uniform apparent brightness from map to map, so that large-scale variations in backscatter are thus suppressed in favor of local features.

Two complete sets of maps were developed. For an over-all view of the radar moon, Figs. 17(a) through 17(j) contain a series of mosaics of the five belts with uniform cartographic projections, one each for the polarized and depolarized backscatter. The polar caps consisting of four ZAC-areas each are included in the high-latitude Lambert projection for the sake of simplicity. The region between latitudes 16°S and 16°N is in the Mercator (equatorial tangent) projection, from 16° to 48° in a Lambert conic projection (intersections at 21° 20' and 42° 40'), and from 48° to 90° in another Lambert conic projection (intersections at 53° 20' and 74° 40'). The coordinate grids on these mosaics are not highly accurate because of distortions in the

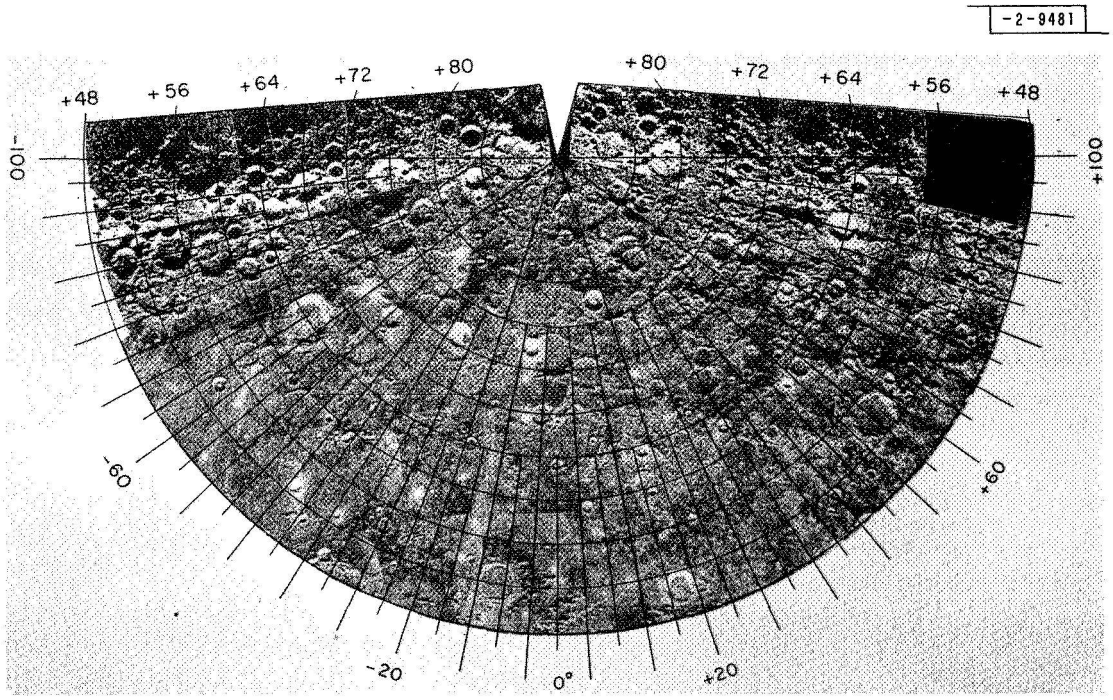

Fig. 17(a). Polarized return, 48°N to 90°N.

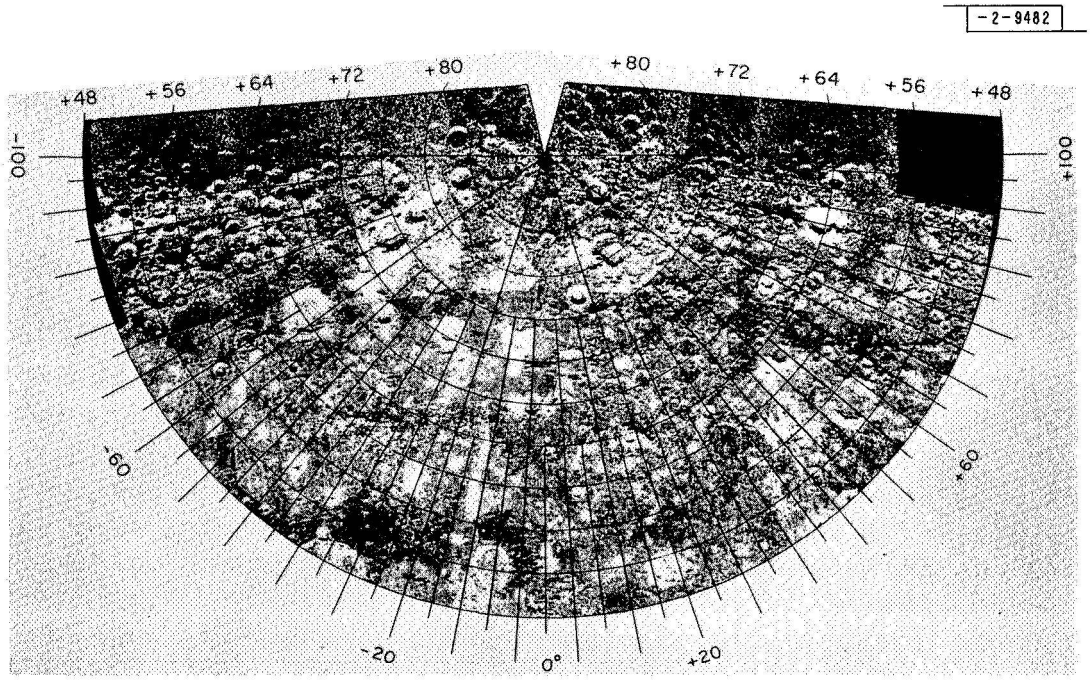

Fig. 17(b). Depolarized return, 48°N to 90°N.

Fig. 17. Lunar radar mosaic finding charts.

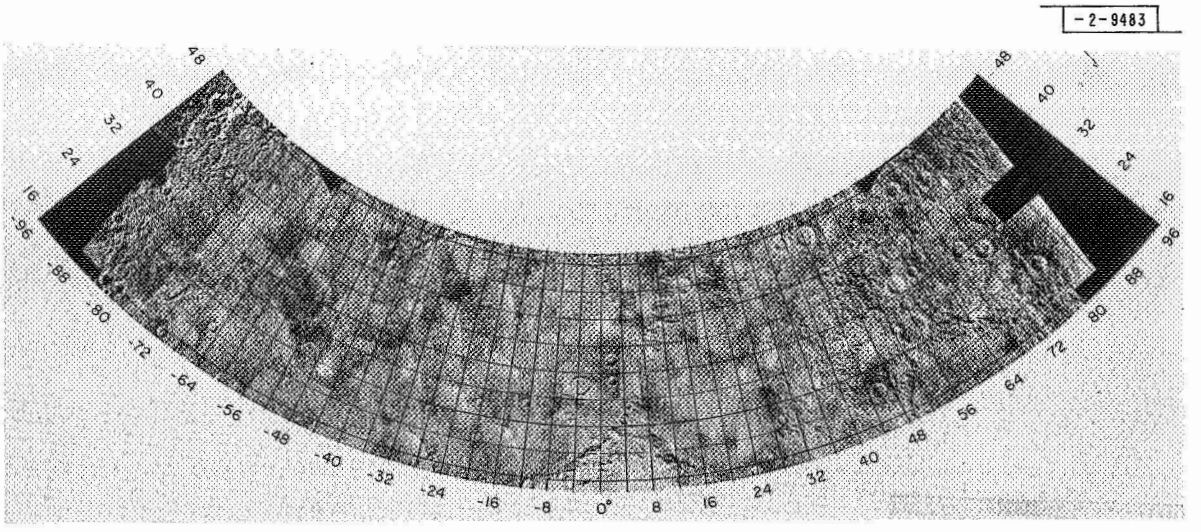

Fig. 17(c). Polarized return, 16°N to 48°N.

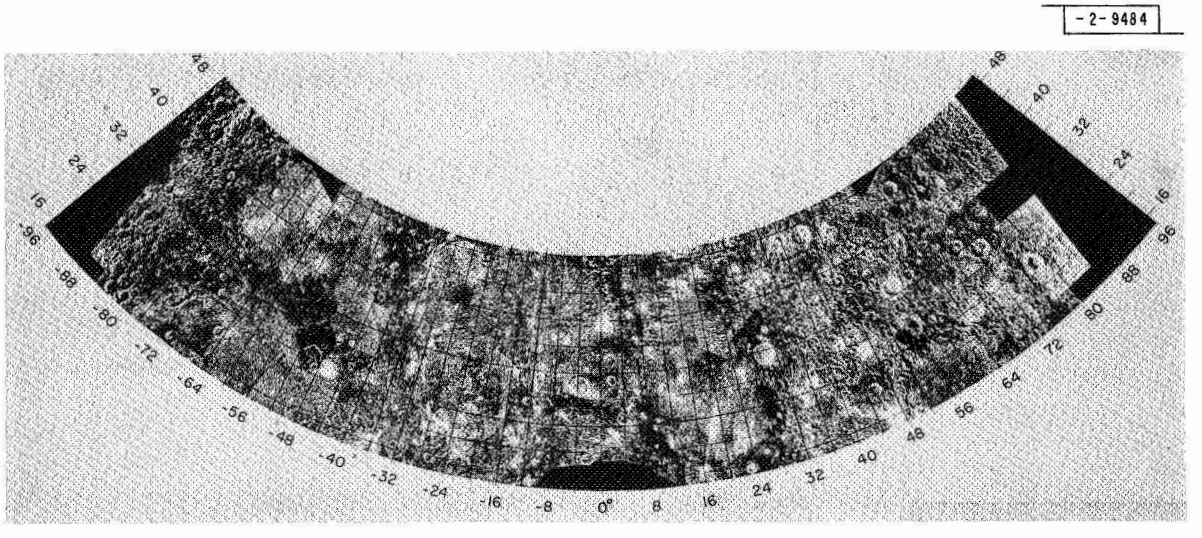

Fig. 17(d). Depolarized return, 16°N to 48°N.

Fig. 17. Continued.

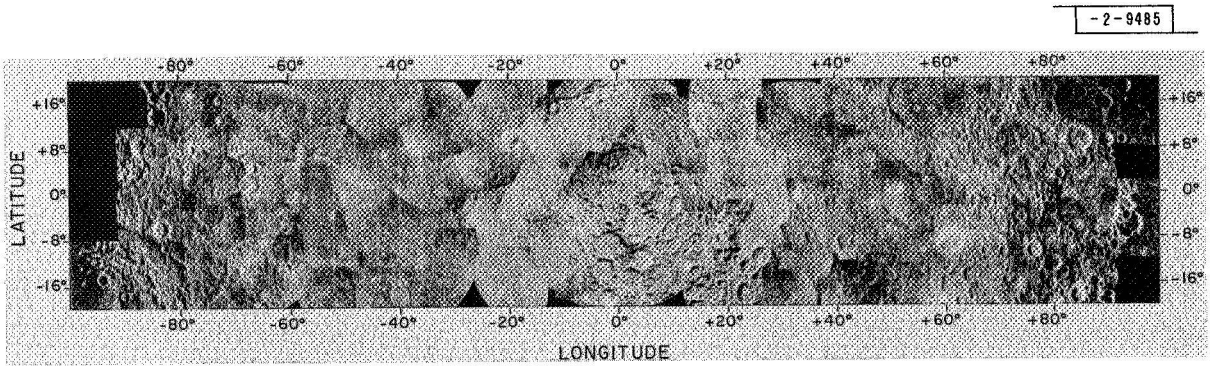

Fig. 17(e). Polarized return, 16°S to 16°N.

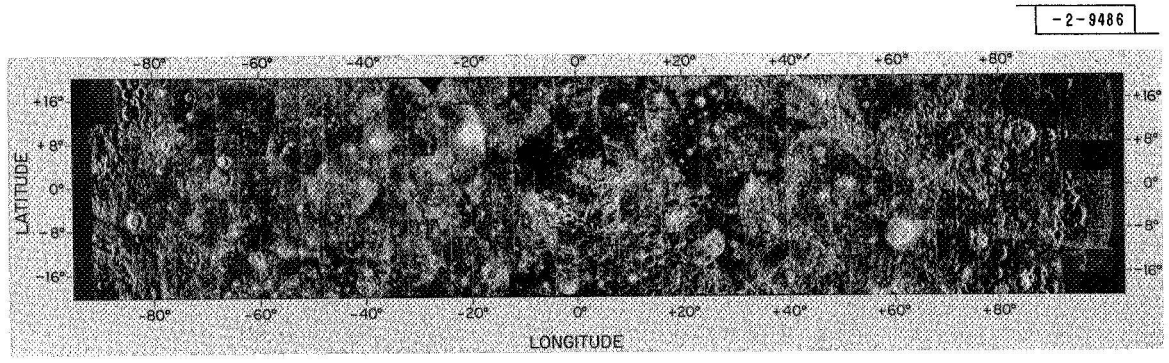

Fig. 17(f). Depolarized return, 16°S to 16°N.

Fig. 17. Continued.

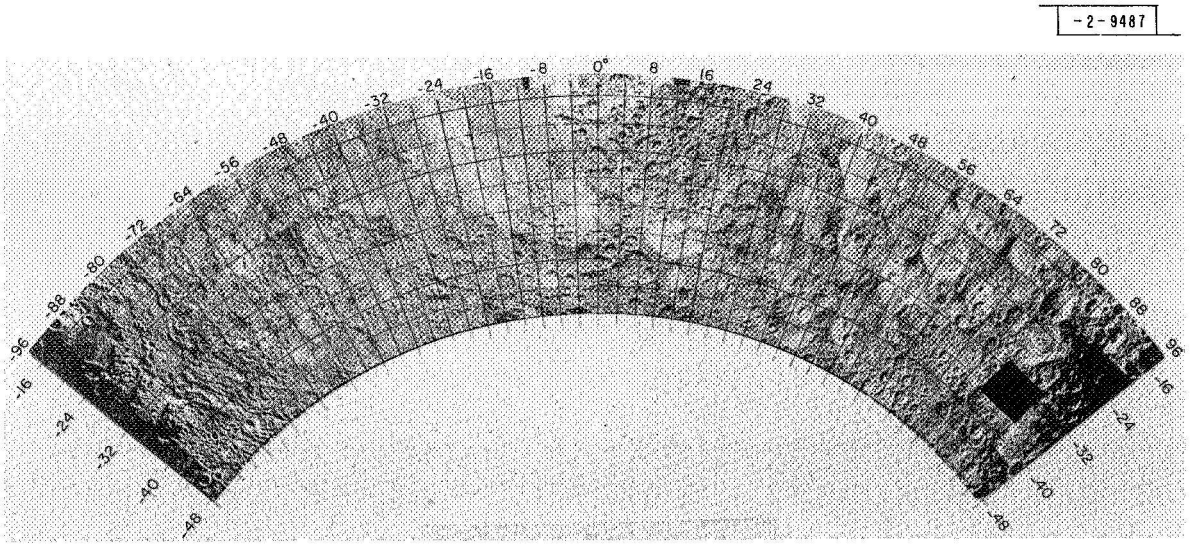

Fig. 17(g). Polarized return, 16°S to 48°S.

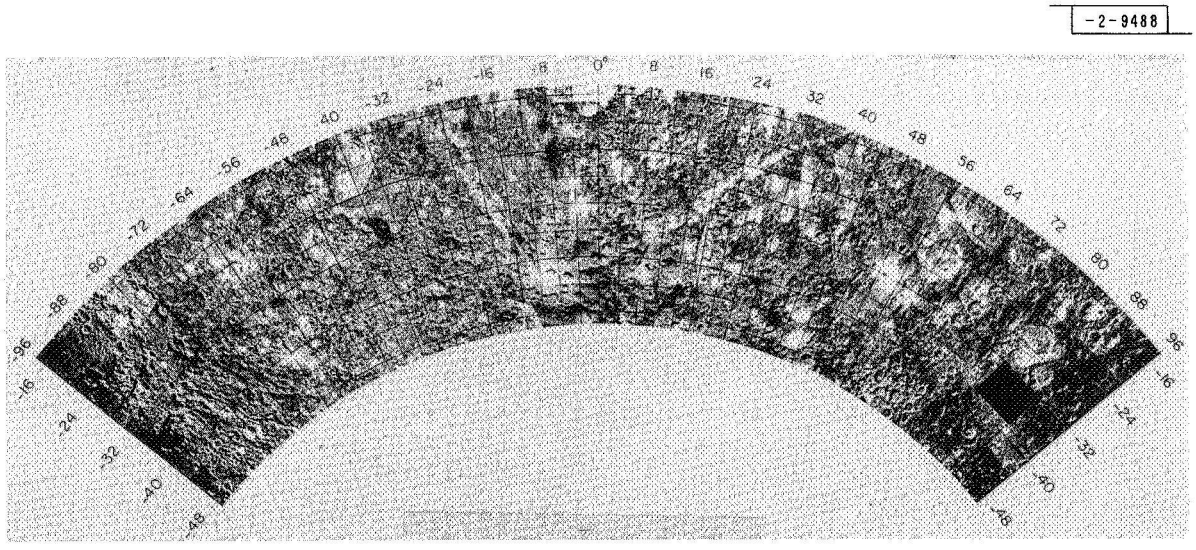

Fig. 17(h). Depolarized return, 16°S to 48°S.

Fig. 17. Continued.

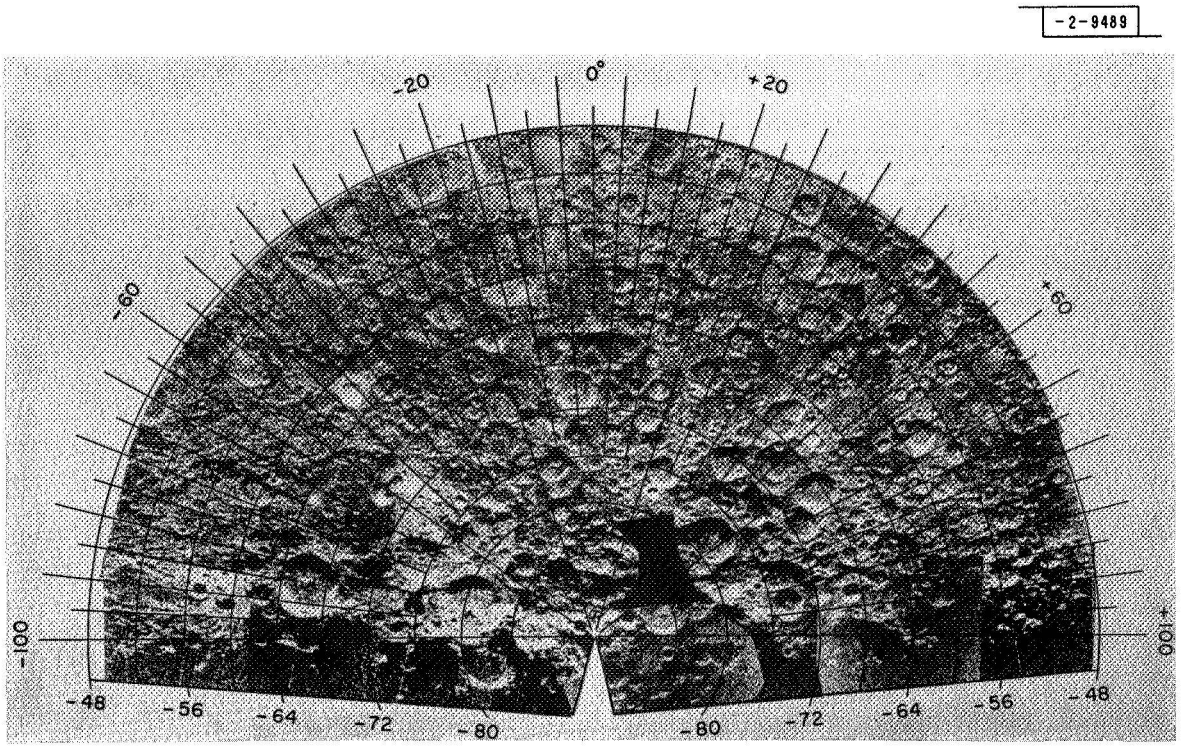

Fig. 17(i). Polarized return, 48°S to 90°S.

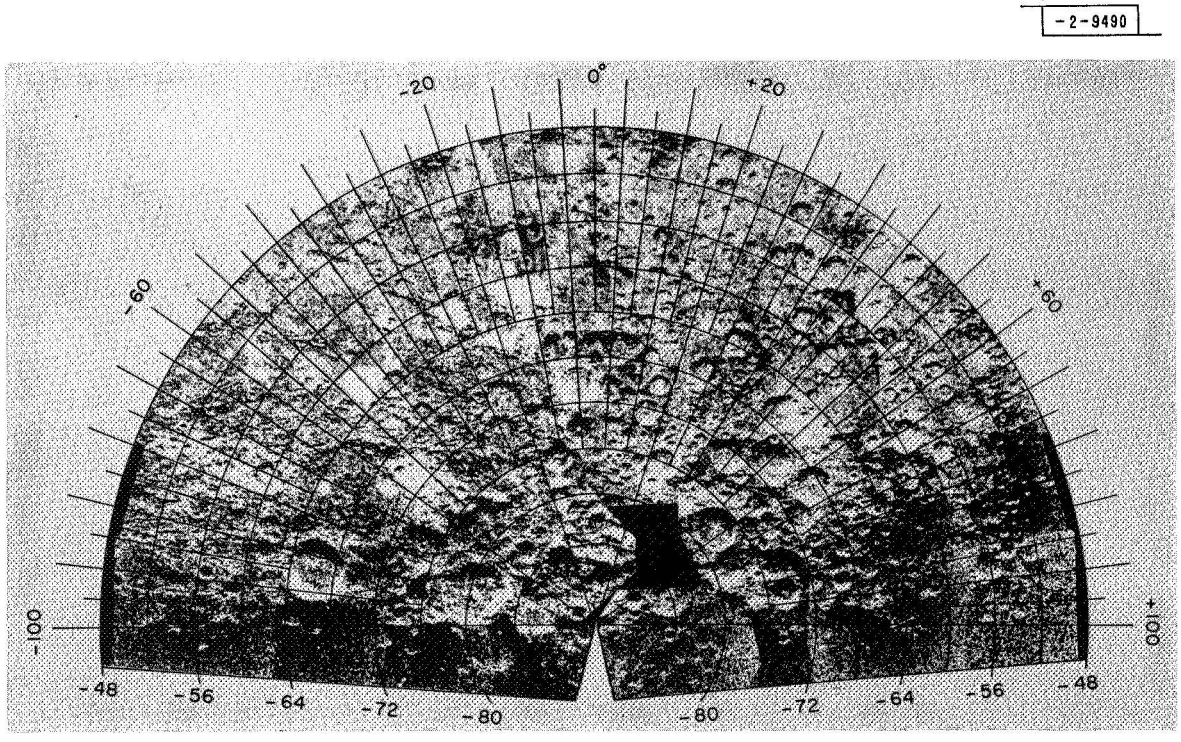

Fig. 17(j). Depolarized return, 48°S to 90°S.

Fig. 17. Continued.

individual ZAC-maps caused by topography and by ephemeris uncertainty (see Sec. II), but serve nevertheless as effective guides in the location of features.

For more detailed investigations, a set of individual ZAC-maps is available in Appendix C,* which is published as an addendum comprising a compendium of 190 actual photographic reproductions. These contain the same backscatter information as the mosaics, but on a larger scale, without the degradation due to halftone printing and with better positional information. The coordinate grids are based on the lunar prediction ephemeris as outlined in Sec. II. Distortions in the radar maps result in positional uncertainties of about 3 to 4 km rms. However, a few areas near the lunar equator have disagreements of as much as 20 km between overlapping areas and their coordinate grids. These result from the greater sensitivity to errors in the lunar ephemeris of the equatorial measurements when the libration axis is of necessity changing rapidly. Additional maps of the ratio of the depolarized/polarized backscatter are included at the end of the Atlas.

B. General Description of the Maps

The significance of the different types of features appearing on the maps has been discussed above, both directly and by inference from the theory. The polarized maps show the quasi-shadowing resulting from local tilts with respect to the mean surface. Superimposed on this relief information are the local enhancements in backscatter, both positive and negative, caused by variations in the roughness or in some cases the dielectric constant of the surface material.

The depolarized maps provide a great deal of additional information. Since the level of the depolarized signal is lower and the slope of the scattering law is less, variations in roughness are more pronounced and are less masked by tilt-caused enhancements. Most craters that are "fresh" in geological appearance show a well-developed halo (of ejecta?) in the depolarized maps. In some cases, the halo is strong enough to obscure on the depolarized map other features that are clear on the polarized map.

There also appear on the depolarized map, and even more distinctly on the ratio map, a number of bright patches – perhaps as many as 1000 on the earthside hemisphere – with diffuse outlines, but no obvious central crater. In all these cases the Lunar Orbiter photographs show a bright, fresh crater or clump of craters at the center of the bright patch, although some of the craters may be only a fraction of a percent of the diameter of the patch. Occasionally, these patches are so bright that they show reasonably well on the polarized maps also; and, in a few cases of identifiable craters, only the bright patch shows on both maps; the pseudo-relief on the crater walls is completely washed out by the rough surface texture (e.g., Messier and Messier A).

Such patches almost certainly indicate a very recent violent event, where the ejected rubble has not been exposed long enough on the surface to be eroded away. For the smallest craters, the event was most likely an impact in a region of shallow regolith. Some of the larger craters are also probably the result of impacting meteorites but others are likely to be of volcanic origin, based on their appearance on the Orbiter pictures. Further investigation of the history of these features is being carried out in cooperation with other researchers but is beyond the scope of the present report.

C. Apollo Sites

We have examined the radar data for most of those sites that have been considered for Apollo landings beyond Apollo 12, with the exception of several of the original mare sites. Our

* Copies of Appendix C are included with all copies of the report provided to NASA. A limited number of copies are available on request from M.I.T. Lincoln Laboratory Distribution Office.

conclusions are presented in the following sections. There appears to be a reasonable correlation between our results and those from other sources, although the descriptions given here are mainly qualitative in nature.

The backscatter maps referred to here will be found in the separately published Appendix C in ZAC-number sequence.

Hyginus Rille: ZAC 2.02, Tape 1 (Central Angle of Incidence = θ = 21.1)

Although the general area is covered by strong radar anomalies (notably the string of craters scattered along the rille), the proposed landing site is on a small area of low radar backscatter and hence apparently has a relatively smooth and rock-free surface. The area of radar darkness coincides with the smooth, dark area on optical photographs and may be either a recent flow or an overlying layer of soil, relatively thick (a meter or more) or compact, since there is no sign on the radar maps of the rocks which presumably have been covered. Examination of the large circular crater at the bend in the rille indicates no unusual rockiness on its floor, but there is quite a strong indication of rockiness in the elongated crater that protrudes northward toward the proposed landing site. This enhancement appears confined to the crater itself and ends with a sharply defined transition to the dark area containing the landing site. There appear to be a number of markedly different geological units available for sampling in a relatively small area.

Descartes: ZAC 2.05, Tape 1 (Central Angle of Incidence = θ = 21.3)

The radar measurements of this site are puzzling, in that the polarized backscatter for the area is well below average, whereas the depolarized is equal to or slightly higher than average. One strong possibility is that the rockiness of the site is about the same as for Apollo 11 and 12 (giving rise to an average depolarized return), but that the soil is much less reflective – perhaps because of a higher porosity – over the entire floor of the large, eroded crater on whose eastern edge the landing site is located.

The two bright, small craters 10 km to the south and 4 km to the northeast show up clearly as strong radar anomalies and should provide an interesting geochemically contrasting surface sample if a traverse were to be extended toward the nearer one.

Davy Rille: ZAC 2.07, Tape 1 (Central Angle of Incidence = θ = 22.3)

This site is located in an area of extremely low radar backscatter. Both polarized and depolarized values are 0.3 times the average for this angle of incidence, which suggests that only a very small percentage of the surface could be rocky, and also that the soil may be unusually porous and consist mainly of low-dielectric-constant minerals. The enchancement along the crater chain of the rille is well marked against such a background, but even these craters exhibit low backscatter values, typically 0.6 times average. It is possible that the craters merely expose the more highly compacted soil some meters below the surface; from the radar results, it appears likely that there is not much rock within the craters either.

Fra Mauro: ZAC 2.09, Tape 1 (Central Angle of Incidence = θ = 18.2)

This is a comparatively featureless area. The polarized backscatter over the 20-km neighborhood is less than half the average for the angle of incidence, indicating a smooth surface, presumably with a thick regolith layer and sparse or heavily eroded surface rocks. There are few indications of recent cratering and even those are relatively subdued. These indications are similar to the Apollo 11 and 12 landing areas, but more extremely subdued.

Hadley-Apennines: ZAC 3.01, Tape 2 (Central Angle of Incidence = θ = 31.0)

This is a complex area on the radar maps. The low (0.5 times average) depolarized return at the proposed landing site itself indicates few rocks, although the optical photos show a substantial amount of cratering. This suggests a thick, eroded regolith layer.

There is a considerable increase in rockiness indicated on the depolarized radar map about 6 to 8 km to the south, and a strong return from the rille itself and from the hills to the east and west.

The polarized return (about 0.9 times average) substantiates the reduced rockiness at the site, but is not so clear about the rille and the surrounding hills, probably because of the rolling nature of the terrain and the resulting variations caused by local surface tilts.

Copernicus: ZAC 3.15, Tape 2 (Central Angle of Incidence = θ = 29.3)

From the radar maps, the proposed landing site appears to be well chosen for the floor of Copernicus, with backscatter values that are near to the lowest in a 20-km circle. These values are nevertheless 1.5 and 3 times the general averages at this angle of incidence for polarized and depolarized radar, respectively, which fact confirms the expectation that the floor of Copernicus will be a very rough area, with a relatively large fraction of the surface covered by exposed and nearly exposed rock. The sizes of these rocks, however, need not be very great to produce the observed radar picture. (The modal values for polarized and depolarized return, within a circle of 20-km radius centered on the proposed landing site, are about 2.3 and 4 times the corresponding general averages, compared with 1.5 and 3 for the landing site.)

Littrow: ZAC 4.04, Tape 3 (Central Angle of Incidence = θ = 41.1)

This area is located on a region with one of the lowest values of depolarized backscatter of the entire 3.8-cm radar map, about 15 percent of the average for its angle of incidence. The Littrow surface should therefore yield a very low fraction of rocks for astronaut sampling. It would be very interesting to discover whether the geochemistry and/or age of the surface material could yield any clue as to the origin of this finely divided or unbroken surface layer, or whether the on-site exploration reveals another unexpected reason for the anomalously weak radar return.

Censorinus: ZAC 4.07, Tape 3 (Central Angle of Incidence = θ = 38.4)

The entire area surrounding the crater exhibits unusually strong enhancement. At the location of the proposed Apollo landing site, the backscatter has dropped well below the extreme value around the crater itself, and is somewhat lower than the average for its angle of incidence. (At the crater both the polarized and depolarized backscatters are about twice the average.) One would expect the surface to be rocky to about the same extent as Apollo 11 and 12 landing sites, or perhaps slightly more. It would be very interesting to obtain a size-distribution count and some sort of "jaggedness factor" for the proposed landing area for the traverses extending toward the crater. This would provide information on the effect of jagged vs smooth rocks on the radar return and might contribute to an improved theory of radar scattering by the lunar surface which could then be applied to the radar data from additional unexplored areas.

Tycho: ZAC 5.16, Tape 5 (Central Angle of Incidence = Θ = 52.3)

At Tycho, the angle of incidence is large (>50°) and interpretation of the radar maps must be carried out with more caution. As pointed out earlier, the effect of local tilts on the backscattered power at such large angles of incidence has become significant in the depolarized map, and must be separated out from the physical character of the surface itself which is of primary concern here.

From both optical and radar pictures, the area surrounding the proposed landing site is relatively flat, and the radar should give a fairly good idea of the surface structure. The polarized and depolarized values are about 1.4 and 1.8 times the average for this angle of incidence, indicating, as expected, that the area is considerably rockier than average. As in the case of the proposed Copernicus landing site, the radar shows that the 2 km × 2 km Tycho site is by far the smoothest for 20 km around. The modal backscatter values elsewhere in the neighborhood are about 2.0 and 2.5 times the corresponding averages.

Marius Hills: ZAC 6.25, Tape 7 (Central Angle of Incidence = Θ = 58.1)

There is no bold relief apparent in this area which might have complicated the interpretation of the radar maps at this high angle of incidence. A number of features show up on both polarized and depolarized radar maps, but none are very strong and the general values of backscatter are about average (1.0 to 1.3 times the average for this angle of incidence). The hills do not appear unusually enhanced, and so should be well covered with soil. There are no indications of large-scale rocky protuberances. From the radar measurements the surface looks somewhat similar to the Apollo 11 and 12 sites, although one must keep in mind that the radar results are not greatly influenced by the chemistry or age of the surface, except indirectly by the state of erosion of surface rocks.

ACKNOWLEDGMENTS

The task of radar mapping of the lunar surface in two polarizations was initiated by G. H. Pettengill (at present at Arecibo Observatory) and carried forward by S. H. Zisk. It received vital cooperation and enthusiasm from many members of the Haystack Research Facility, including G. W. Catuna, H. H. Danforth, J. V. Evans, R. P. Ingalls, M. H. Leavy, J. I. Levine, L. P. Rainville, A. E. E. Rogers, and many others. Special thanks are due to T. Hagfors for making so freely available his time and his extensive knowledge of lunar scattering processes. Modification and new construction of equipment, a necessary preliminary task that is only briefly mentioned in this report, was ably accomplished by W. J. O'Donnell, R. J. Cady, J. M. Sobolewski, and others. Similarly, the development of the voluminous computer programs to plan the measurements and process and display the backscatter data was carried out in large part by R. A. Brockelman, G. W. Armistead, and A. D. Kaminsky.

The completion of this program would have been impossible without the continued guidance and support of P. B. Sebring and M. L. Stone.

The work was provided with financial assistance by NASA under Contract NAS 9-7830.

The cooperation and support of the U. S. Air Force in making available the Haystack Research Facility for the work reported herein is also gratefully acknowledged.

REFERENCES

1. T. Hagfors, "A Study of the Depolarization of Lunar Radar Echoes," Radio Sci. 2, 445-465 (1967).
2. G.H. Pettengill and J.C. Henry, "Enhancement of Radar Reflectivity Associated with the Lunar Crater Tycho," J. Geophys. Res. 67, 4881-4885 (1962).
3. T.W. Thompson and R.B. Dyce, "Mapping of Lunar Radar Reflectivity at 70 Centimeters," J. Geophys. Res. 71, 4842-4853 (1966).
4. G.H. Pettengill and T.W. Thompson, "A Radar Study of the Lunar Crater Tycho at 3.8-cm and 70-cm Wavelengths," Icarus 8, 457-471 (1968).
5. T.W. Thompson, J.B. Pollack, M.J. Campbell and B.T. O'Leary, "Radar Maps of the Moon at 70-cm Wavelength and Their Interpretation," Radio Science 5, 253-259 (1970).
6. J.M. Saari and R.W. Shorthill, "Review of Lunar Infrared Observations," in Physics of the Moon (American Astronautical Society, Tarzana, California, 1967), pp. 57-99.
7. W.J. Eckert, M.J. Walker and D. Eckert, "The Transformation of the Lunar Coordinates and Orbital Parameters," Astron. J. 71, 314-332 (1966).
8. R.F. Scott and F.I. Roberson, "Soil Mechanics Surface Sampler: Lunar Tests, Results and Analyses, Surveyor III Mission Report Part II: Scientific Data and Results," Technical Report 32-1177, Jet Propulsion Laboratory, Pasadena, California (1967).
9. T. Hagfors, J.L. Green and A. Guillen, "Determination of the Albedo of the Moon at a Wavelength of 6 Meters," Astron. J. 74, 1214-1219 (1969).
10. D.F. Winter, "Infrared Emission from the Surface of the Moon," Report D1-82-0717, Boeing Scientific Research Laboratory, Seattle, Washington. To be published in Physics and Astronomy of the Moon, 2nd Ed., edited by Z. Kopal (1968).
11. Iu.G. Matveev, "Reflection and Coefficient for Electromagnetic Waves Incident at Various Angles on a Plane Laminar Medium of Lunite," Astron. Zh. 44, 419-425 (1967).
12. T.V. Tikhonova and V.S. Troitskii, "The Spectrum of the Reflection Coefficient with Changing Lunar Material Properties into the Depth," paper presented at the Symposium on the Physics of the Moon and Planets, Kiev, USSR, 15-22 October 1968.
13. R.D. Davies and F.F. Gardner, "Linear Polarization of the Moon at 6, 11, and 21 cm Wavelengths," Aust. J. Phys. 19, 823-836 (1966).
14. G.L. Tyler, "Brewster Angle of the Lunar Crust," Nature 219, 1243-1244 (1968).
15. L.D. Jafee, C.O. Alley, S.A. Batterson, E.M. Christensen, S.E. Dwornik, D.E. Gault, J.W. Lucas, D.O. Muhleman, R.H. Norton, R.F. Scott, E.M. Shoemaker, R.H. Steinbacher, G.H. Sutton and A.L. Turkevich, "Principal Scientific Results from Surveyor VII; Surveyor VII, A Preliminary Report," NASA SP-173, 1-3 (1968).
16. V.R. Oberbeck and W.L. Quaide, "Genetic Implications of Lunar Regolith Thickness Variations," Icarus 9, 446-465 (1968).
17. W.E. Brown, Jr., "A Lunar and Planetary Echo Theory," J. Geophys. Res. 65, 3087-3095 (1960).
18. D.O. Muhleman, "Radar Scattering from Venus and the Moon," Astron. J. 69, 34-41 (1964).
19. D.G. Rea, N. Hetherington and R. Mifflin, "The Analysis of Radar Echoes from the Moon," J. Geophys. Res. 69, 5217-5223 (1964).
20. J.K. Hargreaves, "Radio Observations of the Lunar Surface," Proc. Phys. Soc. London 73, 536-537 (1959).
21. F.B. Daniels, "A Theory of Radar Return from the Moon and Planets," J. Geophys. Res. 66, 1781-1788 (1961).
22. T. Hagfors, "Some Properties of Radio Waves Reflected from the Moon and Their Relation to the Lunar Surface," J. Geophys. Res. 66, 777-785 (1961).
23. V.A. Hughes, "Diffraction Theory Applied to Radio Wave Scattering from the Lunar Surface," Proc. Phys. Soc. 80, Part 5, 1117-1127 (1962).

24. A.K. Fung and R.K. Moore, "Effects of Structure Size on Moon and Earth Radar Returns of Various Angles," J. Geophys. Res. 69, 1075-1081 (1964).

25. P. Beckman, "Radar Backscatter from the Surface of the Moon," J. Geophys. Res. 70, 2345-2350 (1965).

26. T. Hagfors, "Relationship of Geometric Optics and Autocorrelation Approaches to the Analysis of Lunar and Planetary Radar," J. Geophys. Res. 71, 379-383 (1966).

27. D.E. Barrick and W.H. Peake, "Scattering from Surfaces with Different Roughness Scales; Analysis and Interpretation," Bat-197A-10-3, Batelle Memorial Institute, Columbus Laboratories, Columbus, Ohio (1967), AD 662751.

28. A.H. Marcus, "Application of a Statistical Surface Model to Planetary Radar Astronomy," Technical Report 112, Department of Statistics, The Johns Hopkins University, Baltimore, Maryland (1969).

29. P. Beckmann, "Depolarization of Electromagnetic Waves Backscattered from the Lunar Surface," J. Geophys. Res. 73, 649-655 (1968).

30. A.K. Fung, "Character of Wave Depolarization by a Perfectly Conducting Rough Surface and Its Application to Earth and Moon Experiments," Planet. Space Sci. 15, 1337-1347 (1967).

31. R.D. Kodis, "A Note on the Theory of Scattering from an Irregular Surface," IEEE Transactions on Antennas and Propagation AP-14, 77-82 (1966).

32. D.E. Barrick, "A Note on Scattering from Dielectric Bodies by the Modified Geometrical Optical Method," IEEE Transactions on Antennas and Propagation AP-16, 275-277 (1968).

33. A.K. Fung and H.L. Chan, "Backscattering of Waves by Composite Rough Surfaces," IEEE Transactions on Antennas and Propagation AP-17, 590-597 (1969).

34. D.E. Barrick, private communication.

35. D. Atlas, L.J. Battan, W.G. Harper, B.M. Herman, M. Kerker and E. Matijevic, "Backscatter by Dielectric Spheres," IEEE Transactions on Antennas and Propagation AP-11, 68-72 (1963).

36. J.L. Linsky, "Models of the Lunar Surface Including Temperature-Dependent Thermal Properties," Icarus 5, 606-634 (1966).

37. V.S. Troitskii, "Investigation of the Surface of the Moon and Planets by Means of Thermal Radiation," Proc. Roy. Soc. London, Ser. A296, 366-398 (1967).

38. T. Hagfors, R.A. Brockelman, H.H. Danforth, L.B. Hanson and G.M. Hyde, "Tenuous Surface Layer on the Moon: Evidence Derived from Radar Observations," Science 150, 1153-1156 (1965).

39. A. Rosiwal, "Uber Geometrische Gestemsanalysen. Verhandl. der K.K.," Geol. Reichsanstalt, Wien, 143-175 (1898).

40. J.W. Salisbury and G.R. Hunt, "Infrared Images: Implications for the Lunar Surface," Icarus 7, 47-58 (1967).

41. K.J.K. Buettner, "The Moon's First Decimeter," Planet. Space Sci. 11, 135-148 (1963).

42. J.M. Saari and R.W. Shorthill, "Isotherms of Crater Regions on the Illuminated and Eclipsed Moon," Icarus 2, 115-136 (1963).

43. D.F. Winter, "Transient Radiative Heat Exchange at the Surface of the Moon," Icarus 6, 229-235 (1967).

44. E.C. Roelof, "Thermal Behavior of Rocks on the Lunar Surface," Icarus 8, 138-159 (1968).

APPENDIX A
BEAM-OFFSET CORRECTIONS

Because of apparent electrical mispointing of the radar beam, several of the backscatter maps appeared to be shaded from dark to light in the assumed direction of the mispointing. This effect was later corrected with a computer program that determined the best-fit values for an assumed offset of the Gaussian beam on the celestial sphere. The criterion for the fit was the minimization of the mean-squared-deviation of the backscattered power from a constant. The beam-offset values in degrees of arc are available on the header record for each map (see Appendix B) in an x-y coordinate system tied to the range-Doppler system: The y-axis coincides with the libration axis of the moon on the celestial sphere, and the x-axis is directed at 90° clockwise from it. Values for x and y of the center of the map at the time of the observation are also given, as well as the position angle of the axis of the moon, the angle from the latter to the libration axis, and several other ephemeris quantities. The original values of backscatter may be recovered by appropriate use of these data. The presence of a very bright feature on a few of the maps affected the shading correction.

APPENDIX B
MAGNETIC TAPE FORMAT

The set of ZAC backscatter maps has been made available to NASA on fifteen 2400-foot digital magnetic tapes with appropriate headings and file marks.

Each map begins with a 125-word (plus one Fortran count-word) header record, containing the information in Table B-1. Following the header, there are 201 Fortran (logical) records,* one for each horizontal line of the map, that list the backscatter values. Each logical record contains 201 integer words [in 1's complement, i.e., (all 0 bits) = 0, (all 1-bits) = −0], that represent the normalized, corrected backscatter power levels for each point on the (201 × 201) element map. The value 5000 is the mean for the lunar surface. Small negative values (absolute value less than about 2000) result from noise in the data. Values of −100,000 or −1,000,000 represent points that were not measured or were otherwise excluded from the valid mapped areas. The points are on an evenly spaced square matrix on the LAC-chart cartographic projections listed in the text; the latitude and longitude for the center and four corner points are listed in the header record (Table B-1).

Each ZAC-area is represented by two such maps, the first map being of the polarized return and the second the depolarized return arranged consecutively with individual header records but with no other separation on the tape. Each such ZAC-area is terminated by two end-of-file marks. The end of the data on the tape is indicated by a third end-of-file mark.

The ZAC-areas contained on each tape are listed in Table B-2.

* Note that the maximum length of an unblocked Fortran physical record is 128 words, so that each logical record of 201 words is written as two physical records on the tapes.

TABLE B-1

CONTENTS OF HEADER RECORDS ON MAGNETIC TAPES

Word Number(s)	Contents
1-18	18-word BDC title, containing ZAC-number, date and time of the observation, pulse length, and polarization type.
19, 20	Selenographic longitude and latitude (integer word, in units of 0.01 degree) of the fitted offset of the antenna beam (see Appendix A).
21	No entry.
22	Cartographic projection: 1 = Mercator; 2 = low-latitude Lambert; 3 = high-latitude Lambert; 4 = Polar stereographic (see text).
23, 24(F)*	Selenographic longitude of map center.
25, 26(F)	Selenographic longitude of lower left corner.
27, 28(F)	Selenographic longitude of upper right corner.
29, 30(F)	Selenographic latitude of map center.
30, 31(F)	Selenographic latitude of lower corners.
31, 32(F)	Selenographic latitude of upper corners.
33, 34	No entry.
35, 36(F)	x-value } of the antenna beam offsets in the x-y coordinate system (see Appendix A).
37, 38(F)	y-value }
39-42	No entry.
43-77	Backscatter averages over different subsections of the map.
78	Backscatter average for the entire map.
79-103	No entry.
104	Number of valid points (out of a maximum total number of 40,401) in the map.

The following entries refer to the values of the corresponding quantities at the start of the observing run.

105, 106(F)	Longitude } Selenographic position of the subradar point
107, 108(F)	Latitude }
109, 110(F)	Angle measured clockwise from the moon's North Pole to the libration axis ("Doppler angle").
111, 112(F)	Round-trip radar time delay (in seconds) to the subradar point.
113, 114(F)	Doppler shift of the moon's limb with respect to its center of mass (in Hz) based on 7840.0-GHz transmitter frequency.
115	Topocentric azimuth } (in 0.1 degrees) of the center of the mapped area from the radar.
116	Topocentric elevation }
117	Angle of incidence (in 0.1 degrees) at the center of the map (0 degrees = normal incidence).
118-123	No entry.
124, 125(F)	Position angle of the lunar axis on the celestial sphere (in degrees, counterclockwise from celestial North to the North Pole of the moon).

* The symbol (F) indicates that the quantity is a floating-point value in standard Control Data Corporation CDC-3300 format, which occupies two consecutive 24-bit words on the record.

TABLE B-2

CONTENTS OF MAGNETIC TAPES

Tape Number	ZAC Areas
1	1.01 - 1.05; 2.01 - 2.12
2	3.01 - 3.18
3	4.01 - 4.18
4	4.19 - 4.24; 5.01 - 5.12
5	5.13 - 5.30
6	6.01 - 6.18
7	6.19 - 6.30
8	7.01 - 7.18
9	7.19 - 7.36
10	8.01 - 8.18
11	8.19 - 8.36
12	9.01 - 9.18
13	9.19 - 9.36
14	10.01 - 10.18
15	10.19 - 10.36